

SANDIA REPORT

SAND2005-5742

Unlimited Release

Printed September, 2005

LDRD Project 52523 Final Report: Atomic Layer Deposition of Highly Conformal Tribological Coatings

T.M. Mayer, T.W. Scharf, S.V. Prasad, N.R. Moody, R.S. Goeke, M.T. Dugger, R.K. Grubbs
Sandia National Laboratories

S. M. George, R.A. Wind
University of Colorado

J.M. Jungk, W.W. Gerberich
Univeristy of Minnesota

Prepared by
Sandia National Laboratories
Albuquerque, New Mexico 87185 and Livermore, California 94550

Sandia is a multiprogram laboratory operated by Sandia Corporation,
a Lockheed Martin Company, for the United States Department of Energy's
National Nuclear Security Administration under Contract DE-AC04-94AL85000.

Approved for public release; further dissemination unlimited.



Issued by Sandia National Laboratories, operated for the United States Department of Energy by Sandia Corporation.

NOTICE: This report was prepared as an account of work sponsored by an agency of the United States Government. Neither the United States Government, nor any agency thereof, nor any of their employees, nor any of their contractors, subcontractors, or their employees, make any warranty, express or implied, or assume any legal liability or responsibility for the accuracy, completeness, or usefulness of any information, apparatus, product, or process disclosed, or represent that its use would not infringe privately owned rights. Reference herein to any specific commercial product, process, or service by trade name, trademark, manufacturer, or otherwise, does not necessarily constitute or imply its endorsement, recommendation, or favoring by the United States Government, any agency thereof, or any of their contractors or subcontractors. The views and opinions expressed herein do not necessarily state or reflect those of the United States Government, any agency thereof, or any of their contractors.

Printed in the United States of America. This report has been reproduced directly from the best available copy.

Available to DOE and DOE contractors from

U.S. Department of Energy
Office of Scientific and Technical Information
P.O. Box 62
Oak Ridge, TN 37831

Telephone: (865)576-8401
Facsimile: (865)576-5728
E-Mail: reports@adonis.osti.gov
Online ordering: <http://www.osti.gov/bridge>

Available to the public from

U.S. Department of Commerce
National Technical Information Service
5285 Port Royal Rd
Springfield, VA 22161

Telephone: (800)553-6847
Facsimile: (703)605-6900
E-Mail: orders@ntis.fedworld.gov
Online order: <http://www.ntis.gov/help/ordermethods.asp?loc=7-4-0#online>



SAND 2005-5742
Unlimited Release
Printed October 2005

LDRD Project 52523 Final Report: Atomic Layer Deposition of Highly Conformal Tribological Coatings

Thomas M. Mayer, 6118
Geochemistry Department

Thomas W. Scharf, M.T. Dugger,
and S.V. Prasad, 1824
Microsystems Materials
Department

N.R. Moody, 8754
Microsystems & Materials
Mechanic Department

R. S. Goeke, and R. K. Grubbs, 2452
Thin Film, Vacuum & Packaging
Department

Sandia National Laboratories
PO Box 5800
Albuquerque, NM 87185

S. M. George, and R.A. Wind J. M. Jungk, and W.W. Gerberich
University of Colorado University of Minnesota

Abstract

Friction and wear are major concerns in the performance and reliability of micromechanical (MEMS) devices. While a variety of lubricant and wear resistant coatings are known which we might consider for application to MEMS devices, the severe geometric constraints of many micromechanical systems (high aspect ratios, shadowed surfaces) make most deposition methods for friction and wear-resistance coatings impossible. In this program we have produced and evaluate highly conformal, tribological coatings, deposited by atomic layer deposition (ALD), for use on surface micromachined (SMM) and LIGA structures. ALD is a chemical vapor deposition process using sequential exposure of reagents and self-limiting surface chemistry, saturating at a maximum of one monolayer per exposure cycle. The self-limiting chemistry results in conformal coating of high aspect ratio structures, with monolayer precision. ALD of a wide variety of materials is possible, but there have been no studies of structural, mechanical, and tribological properties of these films. We have developed processes for depositing thin (<100 nm) conformal coatings of selected hard and lubricious films (Al₂O₃, ZnO, WS₂, W, and W/Al₂O₃ nanolaminates), and measured their chemical, physical, mechanical and tribological properties. A significant challenge in this program was to develop instrumentation and quantitative test procedures, which did not exist, for friction, wear, film/substrate adhesion, elastic properties, stress, etc., of extremely thin films and nanolaminates. New scanning probe and nanoindentation techniques have been employed along with detailed mechanics-based models to evaluate these properties at small loads characteristic of microsystem operation. We emphasize deposition processes and fundamental properties of ALD materials, however we have also evaluated applications and film performance for model SMM and LIGA devices.

This page intentionally left blank

Table of Contents

	Project Summary	5
1.	Introduction	6
2.	Atomic Layer Deposition for High Aspect Ratio Structures	7
3.	Growth, Characterization, and Tribological Studies of WS ₂	13
4.	Growth and Characterization of W and W/Al ₂ O ₃ Laminates	26
5.	Fracture of ALD Tungsten Films	32
6.	Properties and Fracture of W/Al ₂ O ₃ Nanolaminates	33
7.	Finite Element Modeling and Properties of Ultrathin ALD Films	41
8.	Summary	56

This page intentionally left blank

PROJECT SUMMARY

This project addresses the issue of lubrication and wear-resistant coatings on microelectromechanical systems (MEMS). Friction and wear are major concerns in the performance and reliability of MEMS devices. While a variety of lubricant and wear resistant coatings are known which we might consider for application to MEMMS devices, the severe geometric constraints of many micromechanical systems (high aspect ratios, shadowed surfaces) make most deposition methods for friction and wear-resistance coatings impossible. In this program we have produced and evaluate highly conformal, tribological coatings, deposited by atomic layer deposition (ALD), for use on surface micromachined (SMM) and LIGA structures. ALD is a chemical vapor deposition process using sequential exposure of reagents and self-limiting surface chemistry, saturating at a maximum of one monolayer per exposure cycle. The self-limiting chemistry results in conformal coating of high aspect ratio structures, with monolayer precision. ALD of a wide variety of materials is possible, but there have been no studies of structural, mechanical, and tribological properties of these films. We have developed processes for depositing thin (<100 nm) conformal coatings of selected hard and lubricious films (Al₂O₃, ZnO, WS₂, W, and W/Al₂O₃ nanolaminates), demonstrated the ability to coat very high aspect ratio structures with these materials, and measured their chemical, physical, mechanical and tribological properties. Major attention has been devoted to deposition and characterization of three materials. WS₂ is a superior solid phase lubricant, W is a hard metallic, wear resistant material, and W/Al₂O₃ laminate films are potential 'superhard' coatings with properties determined by the nanometer length scales of the laminate layers.

We have developed a deposition process for WS₂ using WF₆ and H₂S precursors in a laminar flow ALD reactor. Growth was found to be limited by adsorption and decomposition of WF₆ on most surfaces, and a novel Zn catalyzed deposition method was identified. We propose that WF₆ is partially reduced by Zn or ZnS on the surface, and periodic introduction of (C₂H₅)₂Zn greatly enhances the growth of WS₂. Tribological measurements of WS₂ films show them to have very low friction coefficient, approx. 0.02. Coatings only tens of nm thick can give low friction and increase wear life since sliding is interfacial, i.e., between the transfer film and the wear track on the coating. The hexagonal crystal texture of ALD WS₂ is temperature dependent, but shear-induced reorientation at our high contact stresses assures low friction.

W and W/Al₂O₃ films grown at Univ. of Colorado are shown to also be limited by nucleation of W from WF₆, and extensive studies of W nucleation have detailed the growth process. Very uniform, smooth films of W and laminates result from proper control of nucleation kinetics.

Extensive mechanical property measurements of all ALD films measured detail the modulus, hardness, interfacial strength, and crack and delamination mechanisms for these films. Laminate film properties are shown to be dependent on the length-scale of the individual film thicknesses in the laminate, reflective of the effects of interfaces on the deformation and failure properties of these materials.

A significant challenge in this program was to develop instrumentation and quantitative test procedures, which do not now exist, for friction, wear, film/substrate adhesion, elastic properties, stress, etc., of extremely thin films and nanolaminates. New scanning probe and nanoindentation techniques have been employed along with detailed mechanics-based models to evaluate these properties at small loads characteristic of microsystem operation. We emphasize deposition processes and fundamental properties of ALD materials, however we have also evaluate applications and film performance for model SMM and LIGA devices.

1. INTRODUCTION

Friction and wear are major concerns in the performance and reliability of micromechanical (MEMS) devices. While a variety of lubricant and wear resistant coatings are known which we might consider for application to MEMMS devices, the severe geometric constraints of many micromechanical systems (high aspect ratios, shadowed surfaces) make most deposition methods for friction and wear-resistance coatings impossible. In this program we have produced and evaluate highly conformal, tribological coatings, deposited by atomic layer deposition (ALD), for use on surface micromachined (SMM) and LIGA structures. ALD is a chemical vapor deposition process using sequential exposure of reagents and self-limiting surface chemistry, saturating at a maximum of one monolayer per exposure cycle. The self-limiting chemistry results in conformal coating of high aspect ratio structures, with monolayer precision. ALD of a wide variety of materials is possible, but there have been no studies of structural, mechanical, and tribological properties of these films. We have developed processes for depositing thin (<100 nm) conformal coatings of selected hard and lubricious films (Al_2O_3 , ZnO , WS_2 , W , and $\text{W}/\text{Al}_2\text{O}_3$ nanolaminates), and measured their chemical, physical, mechanical and tribological properties. A significant challenge in this program was to develop instrumentation and quantitative test procedures, which do not now exist, for friction, wear, film/substrate adhesion, elastic properties, stress, etc., of extremely thin films and nanolaminates. New scanning probe and nanoindentation techniques have been employed along with detailed mechanics-based models to evaluate these properties at small loads characteristic of microsystem operation. We emphasize deposition processes and fundamental properties of ALD materials, however we have also evaluate applications and film performance for model SMM and LIGA devices.

2. ATOMIC LAYER DEPOSITION FOR HIGH ASPECT RATIO STRUCTURES

Microelectromechanical systems (MEMS) comprise a variety of functional mechanical devices fabricated on length scales from fractions of a micrometer to millimeters¹. These devices are finding application in a wide variety of technologies, including motion sensing, optical switching and other photonic applications, RF switches and filters, mechanical actuators, chemical sensors, and others. As the size of these devices shrinks, surface to volume ratio increases, and at dimensions typical of MEMS devices, inertial forces become insignificant compared to surface forces acting on these mechanisms². Then interfacial phenomena such as adhesion, friction, and wear can dominate the performance and reliability of MEMS devices. The most sophisticated MEMS devices now in development employ sliding contacts in rotary- or linear-motion structures³, where friction and wear are a major concern.

To mitigate these problems, one can modify the surfaces of MEMS devices with coatings to prevent adhesion, and reduce friction and wear. Previous demonstrations of hard coatings (W⁴, SiC⁵) applied to MEMS devices indicate that increased lifetimes due to a reduction of wear can be achieved. However, the three dimensional structure of MEMS devices makes coating difficult. Freestanding mechanical structures must be coated conformally to avoid stress gradients, and shadowed surfaces must be coated equally as well as exposed surfaces. Many MEMS structures contain contacting surfaces on the underside of mechanical structures, gear hubs, fluid channels, etc. with effective aspect ratio (depth/width of a channel) of up to 100. An effective coating process must be able to transport material into these confined spaces and deposit a film of equal thickness, composition, and properties to that deposited on exposed parts of the device.

Most traditional vapor-phase coating processes (e.g. evaporation, sputtering, chemical vapor deposition (CVD), plasma CVD) are largely line-of-sight techniques and are not capable of conformal coating of high aspect ratio or shadowed structures. Solution-based coating processes are capable of penetrating these confined spaces, however the solvent must wet the surface efficiently to avoid bubble formation. Transport of coating material and by-products is diffusion limited, and solution reactions often must be controlled very precisely in order to obtain the desired film^{6,7}. Many materials of interest simply cannot be deposited in a solution-based process.

We have previously shown that vapor phase deposition of hydrophobic fluorinated alkylsiloxane monolayer films is effective at preventing adhesion in MEMS devices due to water adsorption and capillary condensation⁸. The self-limiting nature of the chemical vapor deposition process used in that work ensured uniform coating of high aspect ratio MEMS structures. In this work we demonstrate the application of a novel chemical vapor deposition process – atomic layer deposition (ALD) – to apply Al₂O₃ wear resistant films of nominally 10 nm thickness on surface micromachined devices. We show that highly conformal coating of microsystem structures is possible, that we can control the stoichiometry and structure of deposited films, and that they are potentially useful as wear resistant coatings on micromachines.

ALD is a chemical vapor deposition process that employs self-limiting surface reactions applied in a binary sequence, leading to atomic layer controlled growth⁹⁻¹¹. The self-limiting surface chemistry permits conformal coating of high aspect ratio structures, with monolayer precision. A binary reaction sequence for deposition of Al₂O₃ using trimethylaluminum and water as precursors is as follows^{12,13}:



where surface species are indicated by the asterisks. Each half reaction involves the reaction between a gas phase precursor and a surface functional group. The surface reaction continues until all functional groups are consumed, and replaced with a new functional group. If the precursor is unreactive with the new surface functional groups the reaction ceases at maximum coverage of one monolayer of reagent per half cycle. Application of the binary sequence ABAB... results in layer-by-layer controlled growth. At an appropriate process temperature where

reactions are self-limiting, and sufficient exposure is allowed to coat all surfaces, deposition is extremely conformal and the process is relatively insensitive to other parameters such as pressure and exposure time.

We deposit films in a viscous flow ALD reactor previously described¹⁴. Precursors are introduced to the hot wall reactor using N₂ as a carrier gas, at a total pressure of approx. 1 torr, and temperature of 168°C. Precursors are injected into the carrier gas stream at their ambient vapor pressure, using pneumatically operated valves. Exposure times for the A and B precursors, and purge times between A and B pulses are independently set. Typical exposure and purge times are 1 and 5 sec., respectively, for a total AB sequence time of 12 sec. Deposition rate is measured using an in-situ quartz crystal microbalance (QCM), and is typically 0.101 nm/cycle for Al₂O₃. Typically the deposition rate per cycle is constant within a run and very reproducible from run to run.

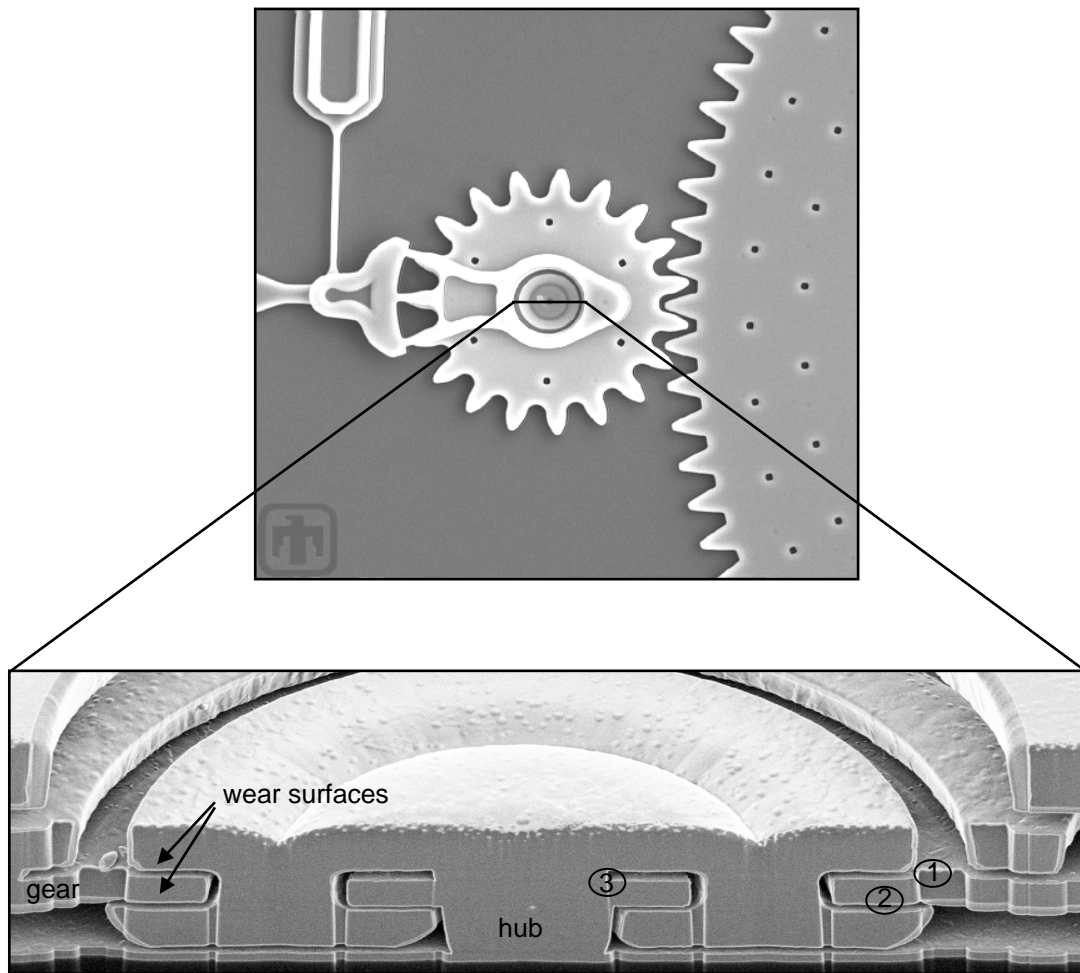


Figure 2.1. (a) MEMS microengine, consisting of a gear turning on a hub. An electrostatic comb-drive actuator (not shown) drives the gear. The structure uses 3 μ m thick polycrystalline Si for mechanical structures. The sacrificial oxide has been removed to release the device. (b) Cross section of the hub showing the contact surfaces of the gear and hub, and the buried channel in the interior of the hub. Locations 1–3 are points of examination of the ALD film by TEM.

Al₂O₃ films were deposited on both flat Si substrates, and on Si MEMS structures. Flat samples were used for thickness and composition measurements by ellipsometry and x-ray photoelectron spectroscopy (XPS). Ellipsometric measurements were consistent with the deposition rate measured by QCM, and with the dielectric function of Al₂O₃ films deposited by other techniques. XPS measurements showed only Al and O, in ratios consistent with Al₂O₃.

The MEMS test structure is a surface micromachined^{3,15} microengine device¹⁶ shown in Figure 1a, fabricated using four levels of polycrystalline Si for mechanical structures separated by sacrificial SiO₂ layers. Patterns are defined by conventional lithography and etching processes. Mechanical structures are finally released by etching the sacrificial SiO₂ layers with HF solution, followed by drying in a supercritical CO₂ drying process. Following release and dry, devices are introduced into the ALD reactor for Al₂O₃ deposition.

Nominally 10 nm of Al₂O₃ was deposited using 100 cycles of TMA/H₂O exposure. Ellipsometric measurements on flat samples indicated actual deposited thickness of 9.7 +/- 0.2 nm. After deposition, a micromachine was cross sectioned for transmission electron microscopic (TEM) inspection, using focused ion beam sputtering to remove a thin section through the hub of the engine. The structure of the hub in cross section is shown in Figure 1b. The deposited film was examined in three locations on this structure, indicated in Figure 1b. Location 1 is on the top of the gear surface, which is exposed by direct line-of-sight to the gas source. Location 2 is on the underside of the gear, shadowed from the gas source, while location 3 is at the end of a long channel inside the hub structure. The channel is approx. 35 μm long and 0.5 μm wide, which, including bends, represents an effective aspect ratio of >100.

TEM micrographs of the film at each of the three locations are shown in Fig. 2. Film thickness at locations 1 and 2 is very near the target thickness of 10 nm, while at location 3, in the buried channel, the film is approx. 10.5 nm. This discrepancy in thickness between the three locations is large for an ALD process. We suspect that the larger thickness in the recessed structure is a result of inadequate purging of the precursor gases in between half cycles of the ALD process. Typically, high aspect ratio structures require somewhat longer purge times to ensure complete transport of reagents into and products out of the confined spaces.

We confirm the composition of the deposited film by energy dispersive x-ray spectrum imaging¹⁷ of the films in the

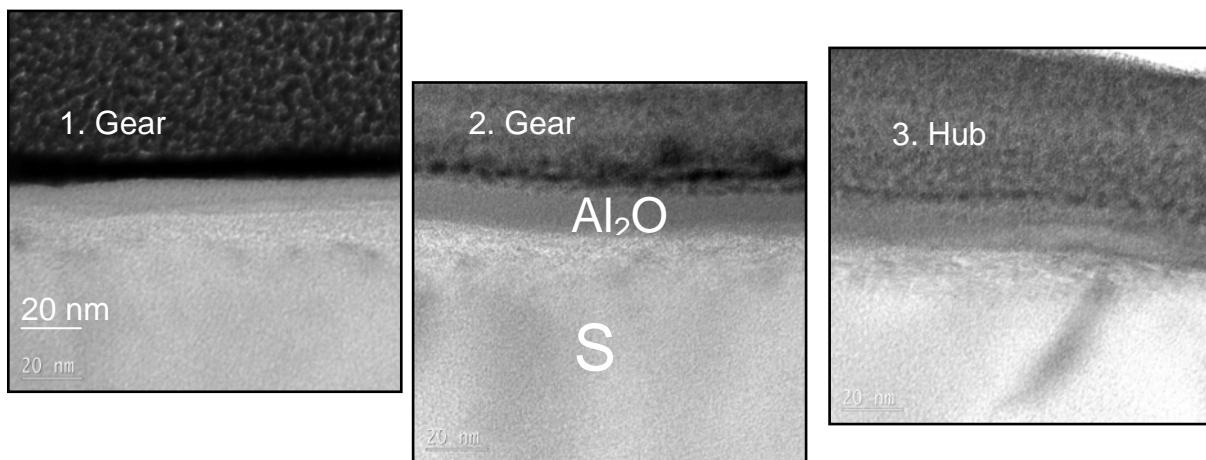


Figure 2.2. TEM cross-section of locations 1 – 3 (from figure 2). Measured film thickness ranges from 10.0 nm at location 1 to 10.5 nm at location 3.

TEM. Results of this analysis are shown in Figure 3, where Si is confined to the substrate (in this case the hub structure), while Al and O are confined to the area of the film. The observed intensity ratio of Al and O in the EDS analysis is consistent with previously measured Al_2O_3 materials, and does not vary with position on the micromachine structure. No elements other than Al and O are observable in the film region. High resolution TEM imaging of the $\text{Si}/\text{Al}_2\text{O}_3$ interface (Figure 4) shows the interface to be abrupt and the alumina film to be amorphous, as expected for deposition at low temperature.

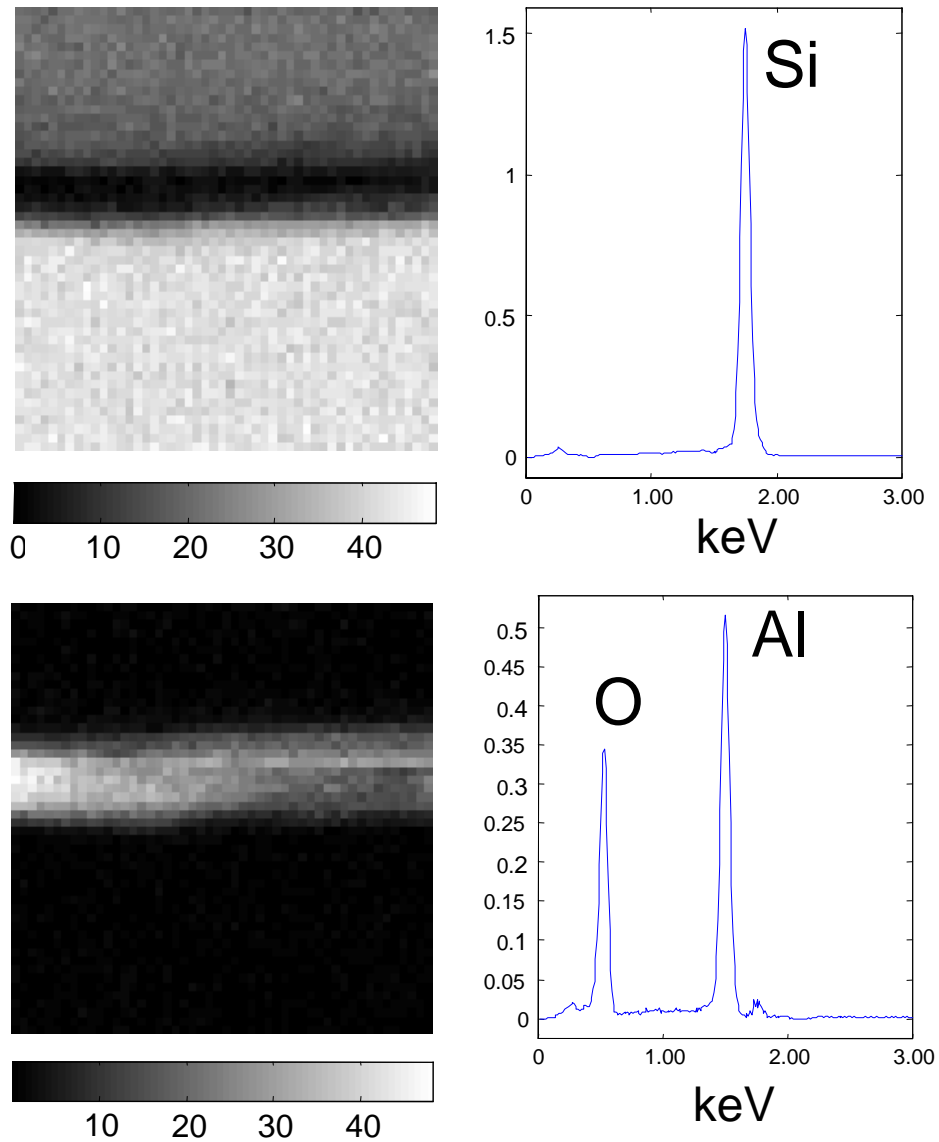


Figure2. 3. EDS spectrum images of the film at the end of the buried channel in the hub (location 3 from figure 2). Component imaging analysis confirms that the film is Al_2O_3 with no other elements present.

Preliminary friction and wear measurements for these 10 nm thick Al_2O_3 films show a friction coefficient of 0.3 for a Si_3N_4 ball sliding on a flat, Al_2O_3 coated substrate, and less wear particle generation than for a native oxide coated Si substrate. We have yet to quantify the nature of the wear and failure process as a function of applied load. Nor have we characterized or optimized the film for device performance. More complete measurements of mechanical and tribological properties of ALD films, and their performance in MEMS devices are in progress and will be reported in future publications.

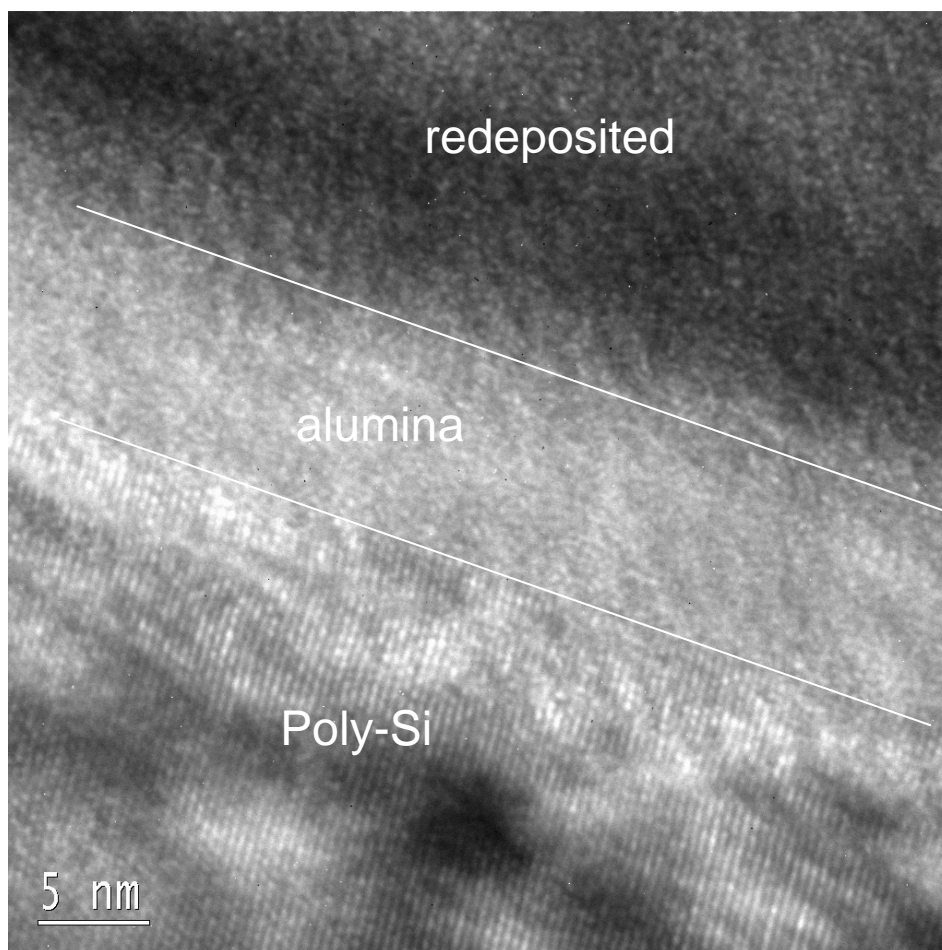


Figure 2.4. HRTEM image of an ALD Al_2O_3 film on polycrystalline silicon MEMS structure. The alumina/Si interface is abrupt and the film is amorphous.

We have shown that ALD is well suited to deposition of friction and wear-reducing films on MEMS structures. Sequential reactant exposure and self-limiting surface chemistry result in exquisite control of deposition rate and film thickness, and extremely conformal coating of high aspect ratio structures. The challenge remains to examine the mechanical and tribological properties of thin ALD films, and their suitability to application in functional MEMS devices. Processes for preparation of a wide range of materials, which are potential hard and/or lubricious

coatings, have been demonstrated by ALD¹⁰. The ease of fabrication of alloys¹⁸ and nanolaminates¹⁹ of ALD materials adds extra dimensions to our ability to tailor the properties of materials for tribological applications.

References

- 1 For a general introduction to MEMS technologies and applications see: *MRS Bulletin*; Vol. 26(4) April (2001).
- 2 R. Maboudian and R. T. Howe, *Journal of Vacuum Science & Technology B* **15**, 1-20 (1997).
- 3 J. J. Sniegowski, M. P. de Boer, *Ann Rev. Mater. Sci*; **30**, 297 (2000).
- 4 S. S. Mani, J. G. Fleming, J. J. Sniegowski, M. P. de Boer, L. W. Irwin, J. A. Walraven, D. M. Tanner, D. A. La Van, *Proc. Mater. Res. Soc.* **605**, 135 (2000).
- 5 C. R. Stoldt, C. Carraro, W. R. Ashurst, D. Gao, R. T. Howe, and R. Maboudian, *Sensors and Actuators A-Physical* **97-8**, 410-415 (2002).
- 6 U. Srinivasan, M. R. Houston, R. T. Howe, and R. Maboudian, *Journal of Microelectromechanical Systems* **7**, 252-260 (1998).
- 7 B. C. Bunker, R. W. Carpick, R. A. Assink, M. L. Thomas, M. G. Hankins, J. A. Voigt, D. Sipola, M. P. deBoer, and G. L. Gulley, *Langmuir* **16**, 7742-7751 (2000).
- 8 T. M. Mayer, M. P. deBoer, N. D. Shinn, P. J. Clews, and T. A. Michalske, *Journal of Vacuum Science & Technology B* **18**, 2433-2440 (2000).
- 9 S. M. George, A. W. Ott, and J. W. Klaus, *Journal of Physical Chemistry* **100**, 13121-13131 (1996).
- 10 M. Ritala, M. Leskela, in *Handbook of Thin Film Materials*; Vol. 1, edited by H. S. Nalwa (Academic Press, San Diego, 2002), p. 103.
- 11 M. Leskela and M. Ritala, *Thin Solid Films* **409**, 138-146 (2002).
- 12 A. C. Dillon, A. W. Ott, J. D. Way, and S. M. George, *Surface Science* **322**, 230-242 (1995).
- 13 A. W. Ott, K. C. McCarley, J. W. Klaus, J. D. Way, and S. M. George, *Applied Surface Science* **107**, 128-136 (1996).
- 14 J. W. Elam, M. D. Groner, and S. M. George, *Review of Scientific Instruments* **73**, 2981-2987 (2002).
- 15 R. T. Howe, *Journal of Vacuum Science & Technology B* **6**, 1809-1813 (1988).
- 16 J. J. Sniegowski and E. J. Garcia, *IEEE Electron Device Letters* **17**, 366-368 (1996).
- 17 P. G. Kotula, M. R. Keenan, and J. R. Michael, *Microscopy and Microanalysis Journal*, in press (2002).
- 18 J. W. Elam, D. Routkevitch, S. M. George, *J. Electrochem. Soc.*, submitted (2002).
- 19 J. W. Elam, Z. A. Sechrist, and S. M. George, *Thin Solid Films* **414**, 43-55 (2002).

3. GROWTH, CHARACTERIZATION AND TRIBOLOGICAL STUDIES OF WS₂

3.1. Introduction

Tungsten disulphide (WS₂) and molybdenum disulfide (MoS₂), which belong to the family of transition metal dichalcogenides, are well known for their solid lubrication. In the WS₂ layered structure, a sheet of tungsten atoms is sandwiched between two hexagonally packed sulphur layers. The bonding within the S-W-S sandwich is covalent, while weak Van der Waals forces hold the sandwich together resulting in interlamellar mechanical weakness. Thus, under a shearing force the basal planes slide back and forth over one another by intercrystalline slip and transfer to the rubbing counterface. These mechanisms for imparting low friction have already been studied in the literature [refs] and low friction coefficients are realized if there is a) the development of a transfer film on the frictional counterface, b) the friction-induced reorientation of the (0001) basal plane of the grains in the interface occurring parallel to the sliding direction (in the transfer film and the coating itself), and c) the absence of contaminants such as oxygen, carbon, and water. Thus, low friction coefficients (0.01 to 0.05 depending upon normal load) of these films are only exhibited in either in an inert gas or in high vacuum [refs]. Since when sliding in humid air, WS₂ loses its lubrication due to W reacting with moisture and oxygen in the environment forming WO₃, a high friction and wear phase.

Thin films of MoS₂ and WS₂ are typically applied by sputter deposition [refs], pulsed laser ablation [refs], burnishing/impingement, evaporation [refs] or chemical vapor deposition [refs], which are essentially either line-of-sight or high temperature processes. With the line-of-sight techniques it is difficult to coat surfaces shadowed from the target, or uniformly coat sidewalls of three-dimensional or high aspect ratio structures. While the CVD techniques can coat shadowed surfaces, the decomposition and condensation of chemical precursors on the surface at higher temperatures limits its application. For applications such as MEMS devices, where dimensions and separation tolerances are small, and aspect ratios are large, these traditional deposition techniques are inadequate. However, atomic layer deposition (ALD), a surface reaction controlled variant of the chemical vapor deposition (CVD) technique, could overcome many of these problems by using sequential introduction of gaseous precursors and selective surface chemistry to achieve atomic scale controlled growth at lower temperatures. Because of the self-limiting nature of ALD, reactions produce films with very uniform thickness even if the flux of vapor is distributed non-uniformly over the surface. This efficient transport of material into confined spaces at low pressure, and sequential introduction of reactants leads to inherently excellent control of film thickness and coverage of high aspect ratio structures [refs]. This makes it ideally suited for coating shadowed surfaces on the underside of moving mechanical assemblies such as MEMS and rolling element bearings (REB). Recently it was reported that 10 nm thick ALD Al₂O₃ films deposited onto high aspect ratio surface micromachined silicon MEMS microengines are highly conformal [Mayer]. The friction coefficient of silicon (measured against a Si₃N₄ counterface in a ball-on-flat configuration) was reduced from ~0.7 to 0.3 as a result of the ALD Al₂O₃ film. However, there is a need for solid lubricant materials like tungsten disulfide (WS₂) for MEMS and REB devices that can provide friction coefficients of ~0.05 and wear life of millions of cycles, but the chemistry needed to grow transition metal dichalcogenide films by ALD is not known. The objective of our study was to evaluate the growth, microstructure, conformality, and tribological (friction and wear) properties and mechanisms of ALD WS₂ solid lubricant films.

3.2. Experimental Details

ALD viscous flow reactor

WS₂ thin films were grown by sequential reaction of gas precursors WF₆ and H₂S at a total pressure of 1 – 2 Torr, and temperature range of 300 to 350°C in a homebuilt hot-wall viscous flow ALD reactor using N₂ as a carrier and purge gas shown in Fig. 1 [Elam]. Precursors were injected into the carrier gas stream using pneumatically operated valves. More complete details of the viscous flow reactor design can be found elsewhere [Elam, Mayer]. The films were deposited on UV ozone cleaned Si (100) with native oxide (~1.8 nm thick), thermally grown SiO₂, 440C stainless steel coupons, and poly-silicon MEMS test structures coated with ALD Al₂O₃.

Material Characterization Techniques

Site-specific TEM specimens were prepared with a FEI DB-235 dual-beam focused ion beam (FIB)/SEM. The wear track was readily identified with the SEM and the FIB was then used to prepare one TEM specimen along the direction of wear within the wear track and a second specimen outside the wear track. Both specimens were then analyzed in a FEI Tecnai F30-ST TEM/STEM operated at 300kV and equipped with an energy-dispersive x-ray spectrometer (EDXS). X-ray spectral images, where an entire spectrum is acquired from each of series of points in a 2D array, were collected from both the wear surface and the unworn surface specimens. Sandia's Automated eXpert Spectral Image Analysis (AXSIA) software [P.G. Kotula, M. R. Keenan and J.R. Michael, (2003) *Microsc. Microanal.* 9 1-17] was then used to analyze the data. AXSIA quickly reduces large raw spectral images into a compact solution consisting of a small number of linearly independent component image/spectrum pairs. For display purposes the component images are often combined into an RGB color overlay. The same procedure was followed to determine the conformality of ALD WS₂ coated buried MEMS surfaces by FIB cutting through a MEMS structure and extracting a TEM specimen.

Friction and Wear Testing

Friction measurements were made on planar surfaces using a ball-on-disk linear wear tester. The tests were performed in unidirectional sliding mode. The wear tester has the capability to evaluate the friction characteristics in specific locations down to approximately 1 mm track lengths. The tester was housed in an environmental chamber. Oxygen content in the chamber was measured using a Delta F Platinum Series oxygen monitor, and the humidity was monitored by measuring the dew point. Tests were conducted in dry nitrogen (<1% RH, <10 ppm O₂ and <100 ppm H₂O) using a 3.175 mm diameter Si₃N₄ ball (Hoover Precision Products) at normal loads of 98 or 980 mN. These loads correspond to maximum Hertzian contact stresses of ~0.4 and 0.8 GPa, respectively. A 500mN transducer (Sensotec) in the load arm measured the tangential load over a track distance of 1.6 mm. The sliding speed was 3.3 mm/s. The ratio of tangential to normal load is the coefficient of friction (COF). Friction and wear tests were run for either 1000 or 2000 unidirectional cycles.

3.3. Results and Discussion

Film chemistry and growth

WS₂ ALD is based on the CVD reaction:



where WF₆ and H₂S are gas precursors one and two. This reaction is divided into the following two proposed WF₆ and H₂S half-reactions:



where * indicates a surface species. We do not know the precise identity of the surface species present, so the stoichiometry of equations (2) and (3) is undetermined. The exposure time was 2 s and the purge times were 5 and 25 s for WF₆ and H₂S, respectively, at a total pressure of 2 Torr. Initial results using *in situ* QCM showed that WS₂ did not grow on the quartz crystal based on the above processing conditions, and no growth was evident on any of the aforementioned substrates when removed from the reactor at temperatures of 300°C or 350°C. Thus, a chemical precursor was needed to promote the adsorption and reaction of the WF₆ precursor to commence nucleation and growth of WS₂. Diethyl zinc (DEZ) liquid precursor, a known reducing agent for ALD TaN films [Ritala], was chosen as the catalytic material to act as a reducing agent for WF₆ under the following proposed reaction scheme:



Based on equation (5), DEZ pulsed for 2 s and purged for 10 s resulted in the formation of zinc bound to fluorine at the substrate-film interface as determined by x-ray photoelectron spectroscopy (XPS). ZnF₂ formed is then reduced back to Zn (or converted to ZnS) by exposure to H₂S. This catalytic action of Zn in WS₂ is critical for the ALD process, without it no nucleation and growth of WS₂ occurs. The recipe used to grow WS₂ films for this study was one pulse of DEZ for every 50 cycles of WF₆ and H₂S, repeated 5 times to obtain film thickness from 10 to 250 nm

on Si (or SiO₂) and stainless steel surfaces, which are the substrates used in MEMS and rolling element bearings (REB) applications, respectively.

Previous results confirmed WS₂ films nucleated readily on a 3 nm thick ALD ZnS surface grown by sequential reaction of DEZ and H₂S [JMR] at 300°C. The sequential growth of ALD ZnS and WS₂ on a 10 nm thick SiO₂ coated QCM crystal showed that WS₂ did not initially grow on SiO₂, but growth commenced immediately on ZnS. It was also shown that the growth of WS₂ was not constant, but slowed with time. However, even 1 cycle of ZnS growth was adequate to restore high WS₂ growth when its growth began to slow down. Furthermore, it was determined too much DEZ and H₂S precursors (≥ 20 cycles) resulted in ZnS segregation from the interface to the surface, which is not a low friction phase. Note that the most common way to refer to the amount of material deposited per reaction cycle in ALD literature is “growth rate (amount/cycle).” However, this term is non-standard since the amount of material deposited per reaction cycle is no rate. Thus the more accurate term “growth per cycle”, adopted in 1986 by Goodman and Pessa, was used in this work.

Figs. 2(a) and 2(b) show *in situ* quartz QCM measurements detailing the growth enhancement of WS₂ with DEZ precursor. Similar to ZnS (precursors DEZ and H₂S) catalysis, Fig. 2(a) shows that the growth of WS₂ is not constant, but slows with time. From the shaded region in Fig. 2(a), shown in more detail in Fig. 2(b), one 120 mTorr pulse of DEZ was adequate to restore higher WS₂ growth when its growth began to slow down to ~ 0.1 Å/ALD cycle. The overall Zn-catalyzed WS₂ growth was ~ 1.0 Å/ALD cycle. Since growth enhancement of WS₂ is proportional to the amount of Zn deposited, the deposition process is no longer ALD self-limiting. Fig. 2(c) illustrates the Zn catalyzed adsorption and reaction process of WF₆ with products formed. Fig. 3 shows AES depth profiles of WS₂ films deposited by (a) ALD reaction and (b) CVD reaction (no separation of WF₆ and H₂S precursor pulses). The same recipe in the experimental section was used for both reactions outside of the separation of precursors. The purpose of growing the CVD WS₂ film was to determine any differences in chemical constituents between its reactions and ALD, such as decomposition of chemical precursors. Fig. 3 shows elemental tungsten, sulfur, and zinc through thickness of both films, however quantifying the film stoichiometry remains difficult when depth profiling through the films due to preferential sputtering of sulfur, i.e. sulfur is being removed faster than tungsten. The main difference between the reactions is carbon can be seen through thickness of the CVD WS₂ film, likely as a result of the DEZ precursor not breaking down during the reaction and/or carbon byproducts was not desorbed from the surface.

Film microstructure

X-ray diffraction measurements (Fig. 4) confirmed that the ~ 30 nm thick WS₂ films were indeed crystalline with predominantly hexagonal (002) texture grown at (a) 300°C and (b) 350°C. Curved basal planes, orientated perpendicular (100) and at 45° (101) to substrate, are also seen at 350°C, while at 300°C the basal planes are primarily orientated parallel to the substrate, typical of metal dichalcogenide film growth. CVD MoS₂ films exhibited similar growth directions as a function of processing temperature [More]. Fig. 4 also shows corresponding SEM images of the WS₂ films confirming the basal plane orientation differences. The perpendicular-orientated basal planes have approximate growth dimensions of 50 to 100 nm on edge length, while the parallel-orientated basal planes have growth dimensions of approximately 40 to 70 nm on flat. These basal planes exhibit easy shear and sliding between unit cells (shown in inset of Fig. 4) necessary for low friction and wear.

Film tribology

WS₂ films grown on stainless steel and SiO₂ substrates exhibit extremely low friction coefficients, 0.01 to 0.02, under both low (0.4 GPa) and high (0.8 GPa - shown in Fig. 5) contact stresses compared to their respective substrates. The perpendicular basal planes bend under shear loading and thus are re-orientated flat and transfer to the rubbing counterface (inset Fig.5) assuring low friction at our high contact stresses. Perhaps a surface force apparatus with much lower contact stress, typically ≤ 200 MPa, could detect friction differences with perpendicular-orientated basal planes [Israechivilli]. In humid environments with the presence of water vapor and oxygen, WS₂ films lose their lubricating behavior due to the generation of WO₃, a high friction/wear phase, at the sliding interface [refs.]. In addition, slightly higher friction coefficients were measured with the CVD WS₂ film (~ 0.07 - 0.09) in Fig. 3(b). The reason for the higher friction may be due to the AES determined carbon through thickness of the film

which is not acting as a lubricant. Further microscopy and spectroscopy work needs to be done to determine the role of carbon.

Fig. 5(a) shows the friction coefficient decreased as normal load increased at constant velocity according to $\mu = L^{-0.32}$, in good agreement with the Hertzian contact model ($L^{-1/3}$). Linear regression for μ vs. Hertzian pressure fitted to $\mu = (S_0/P) + \mu_0$, gave mean values of shear strength, S_0 , (velocity accommodation parameter) of 35 MPa. μ_0 represents the pressure dependence of shear strength, and is the lowest attainable friction coefficient.

Fig. 6(a) shows an SEM image of inside and outside the wear track (from the test in Fig. 5) for WS_2 on SiO_2 substrate grown at $300^\circ C$. Also shown inside the wear track is the location of where the FIB-cut was taken to prepare a TEM specimen. Fig. 6(b) shows the AXSIA results of the STEM x-ray spectral images of this specimen along with a separate specimen taken outside the wear track, i.e. unworn film. The RGB color overlay shows all of the component images with the WS_2 film in red, Zn-containing regions at the film substrate interface (ZnO and ZnF_2) as well as some clusters scattered through thickness in blue, and the underlying SiO_2 substrate is shown in green. The corresponding EDS x-ray spectra for each component are also shown in Fig. 6(b). It is evident that inside the wear track, approximately half of the WS_2 film was removed as a result of wear and material being transferred to the Si_3N_4 rubbing counterface, which is a necessary mechanism during interfacial sliding to achieve low friction and wear. The low interfacial shear between the transfer film and the underlying wear track provides a longer wear life. This transfer film protection mechanism during interfacial sliding is well known for solid lubricant coatings such as metal dichalcogenides [refs.] and diamond-like carbon coatings [refs.]. One of the drawbacks for any solid lubricant coating is they can eventually wear out (coating and/or transfer film), and further tests are ongoing to determine critical coating thicknesses for operation in MEMS velocity and contact pressure regimes.

Films applied to MEMS

Fig. 7(a) shows an HRSEM image of a poly-silicon MEMS (Summit IV process[®]) pull tab test structure which exhibits high aspect ratio buried and shadowed surfaces. Fig. 7(b) shows a cross-section of a focused ion beam cut taken from the same poly-silicon MEMS pull tab, which was coated with ALD WS_2 film ($300^\circ C$) on top of an ~ 200 nm thick ALD Al_2O_3 film ($180^\circ C$), to see if the film coated the MEMS structure uniformly and conformally. Fig. 7(c) shows a higher magnification of the most buried surface in the test structure. The ALD films coated the whole test structure with conformal Al_2O_3 and ~ 8 nm thick WS_2 . Smooth interfaces are seen between the poly-silicon/ALD Al_2O_3 and ALD Al_2O_3 /ALD WS_2 films. Re-deposit material (Ga and Pt) from the FIB-process is also shown. Fig. 7(d) shows a HRTEM image of the ~ 8 nm thick ALD WS_2 film. The lamellar structure, typical of metal dichalcogenide growth, is clearly seen with basal planes oriented flat to the underlying ALD Al_2O_3 film. It was further determined the interlamellar d-spacing for the (002) was $\sim 5.9 \text{ \AA}$ in good agreement with referenced 6.1 \AA of WS_2 unit cell dimension shown in Fig. 4 inset. The reason for using ALD Al_2O_3 film, known to resist HF vapor, on poly-silicon is apparent when looking at Fig. 8 (a). Without the Al_2O_3 film protecting the poly-silicon MEMS structure, fluorine (HF vapor byproduct and ZnF_2) etch the whole structure. The attack is evident at the poly-Si/ WS_2 interface that looks like film debonding, which TEM determined was a porous, crystalline layer which mainly consisted of ZnF_2 . CVD W deposition also had a similar effect of preferential etching the grain boundaries (worm-holes) on poly-silicon MEMS [Mani]. Fig. 8(b) shows how this vapor etching can be prevented by depositing a ~ 200 nm thick ALD Al_2O_3 film. In addition, the micrographs in Fig. 8 show the Zn-catalyzed WS_2 film, grown under the same process conditions, is considerably thicker on poly-silicon (~ 165 nm) than on Al_2O_3 film (~ 8 nm). The reason is not yet determined but may be a result of the electrical conductivity differences between insulating, semi-conducting, and conducting substrates or the result of vapor etching the underlying substrate. More *in situ* QCM measurements are currently ongoing and will be reported in a separate paper.

3.4. Conclusions

ALD is capable of depositing low friction (COF ~ 0.02) and conformal solid lubricant WS_2 films on high aspect ratio MEMS devices. Zn catalyzed adsorption and reaction of WF_6 greatly increases the growth. Coatings only tens of nm thick can give low friction and increase wear life since sliding is interfacial, i.e., between the transfer film and the wear track on the coating. The hexagonal crystal texture of ALD WS_2 is temperature

dependent, but shear-induced reorientation at our high contact stresses assures low friction. The development of ALD solid lubricant films is expected to enable the application of low friction and low wear films to moving mechanical assemblies such as MEMS structures and REB devices

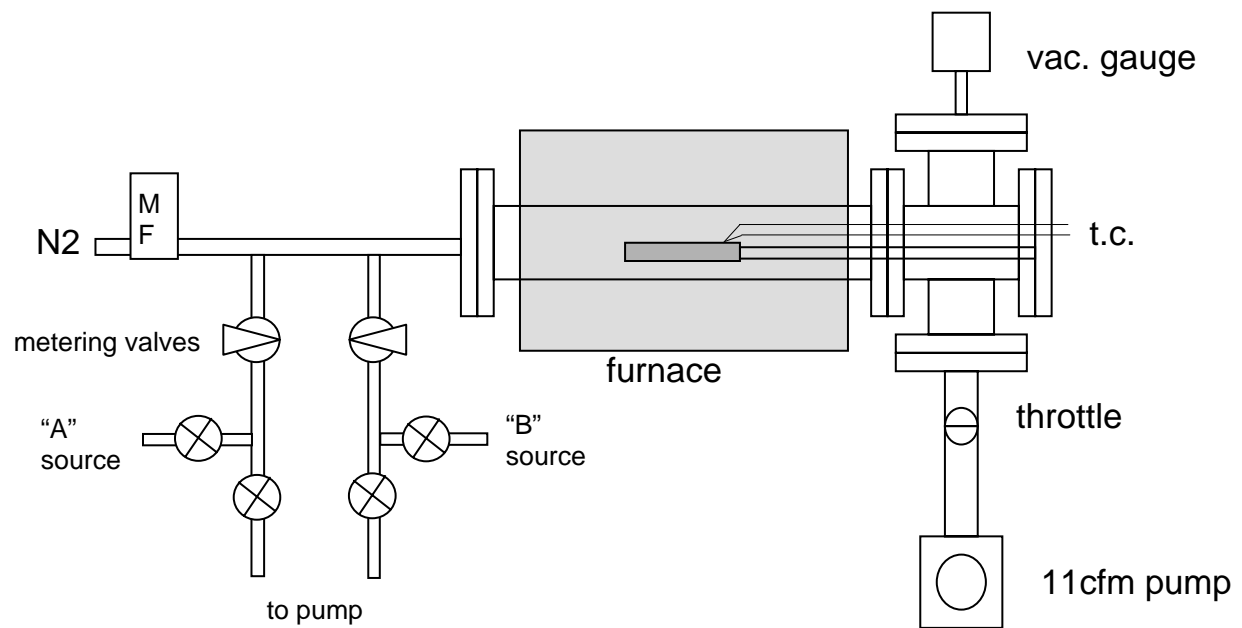


Fig. 3.1 Schematic of viscous flow ALD reactor

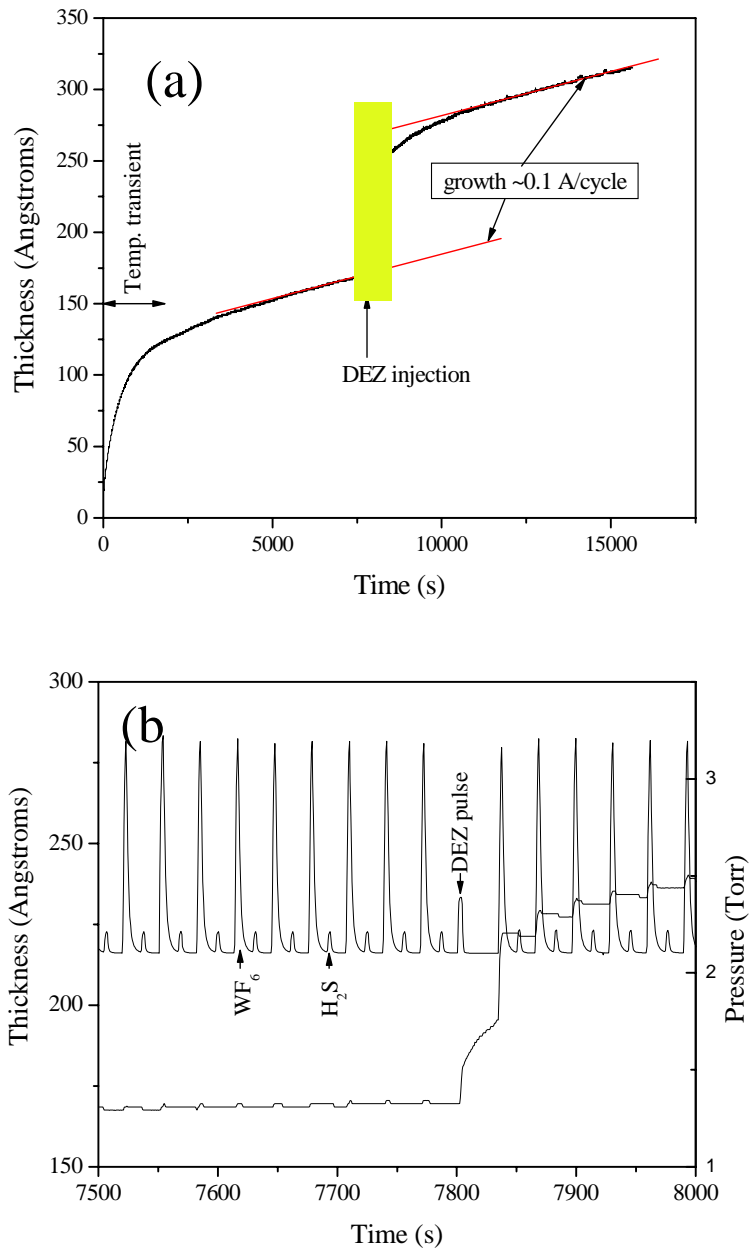
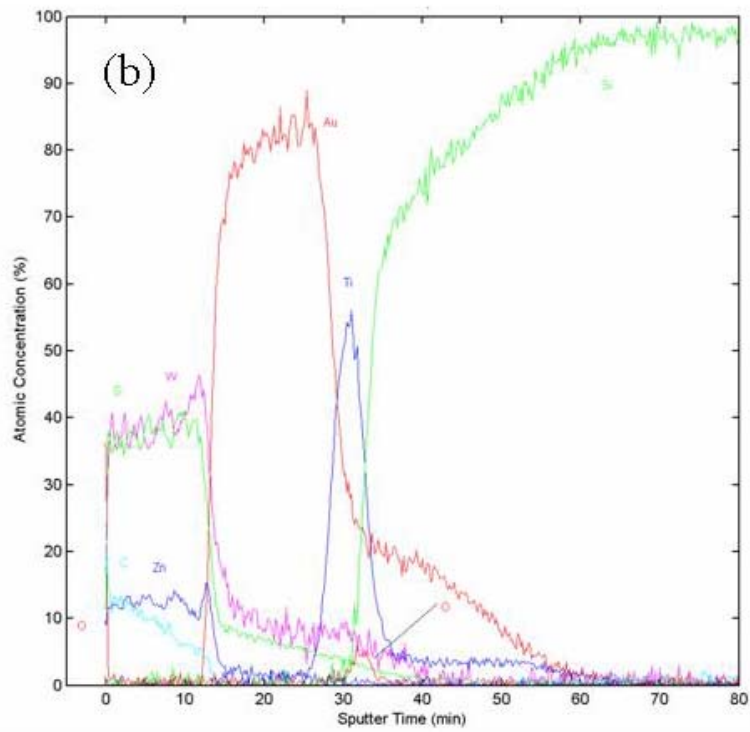
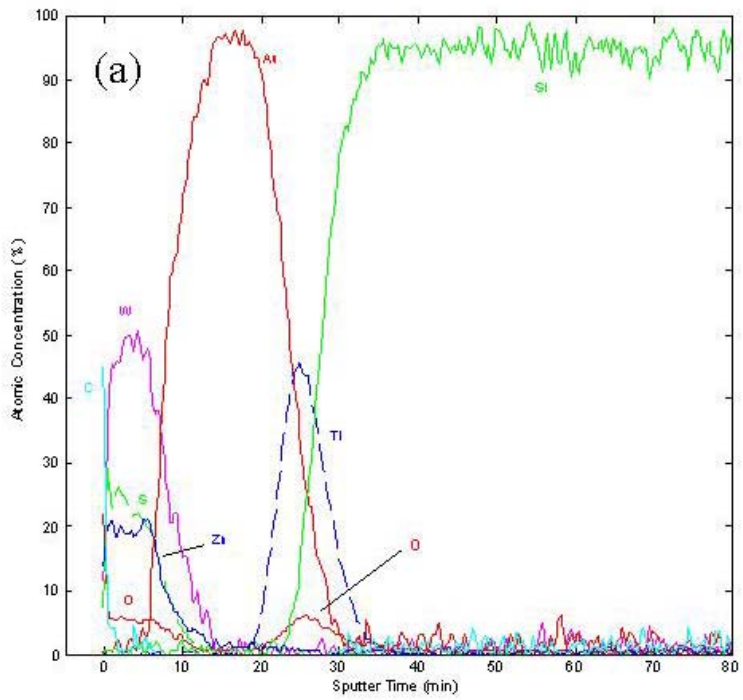


Fig. 3.2a *In situ* QCM growth kinetics of ALD Zn-catalyzed WS₂ over (a) long time, and (b) shorter time (shaded region in (a)) showing how one pulse of DEZ greatly increases WS₂ growth. (c) Cartoon showing Zn catalyzed adsorption and reaction of WF₆ with products formed.



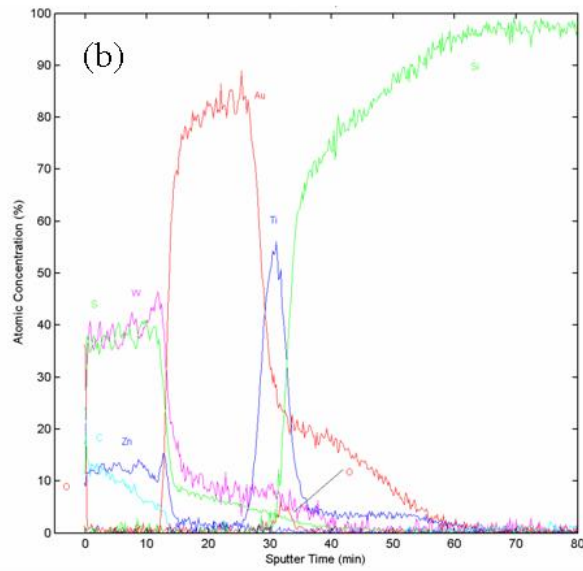


Fig. 3.3. AES depth profiles of (a) ALD WS_2 and (b) CVD WS_2 thin films.

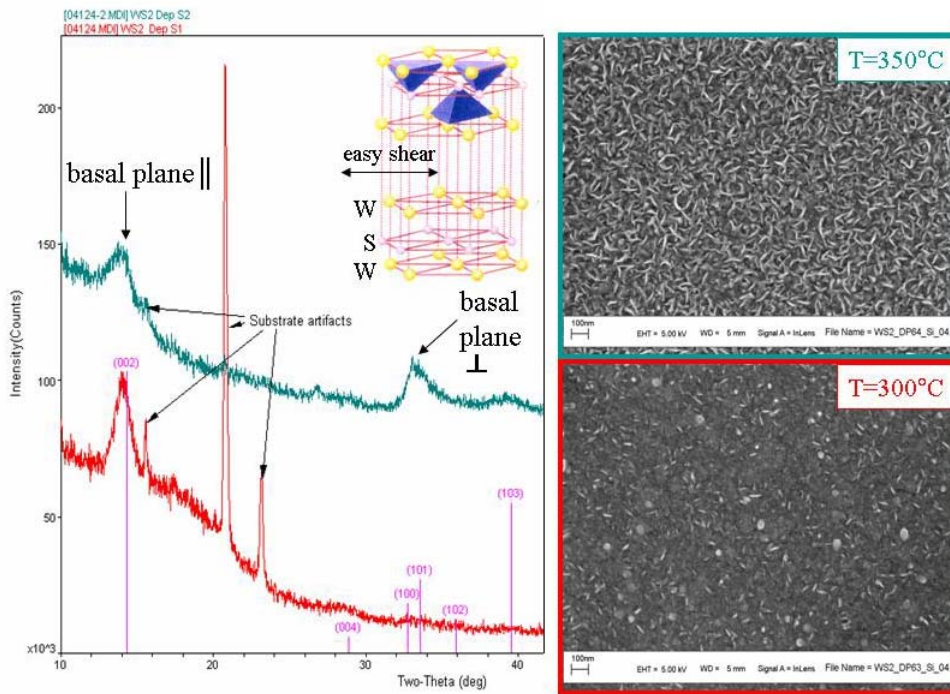


Fig. 3.4. XRD of ALD grown WS₂ (thickness~30 nm) on silicon. SEM image of ALD grown WS₂ film showing predominantly curved basal planes orientated perpendicular to substrate. Inset shows unit cell of WS₂ with easy shear plane.

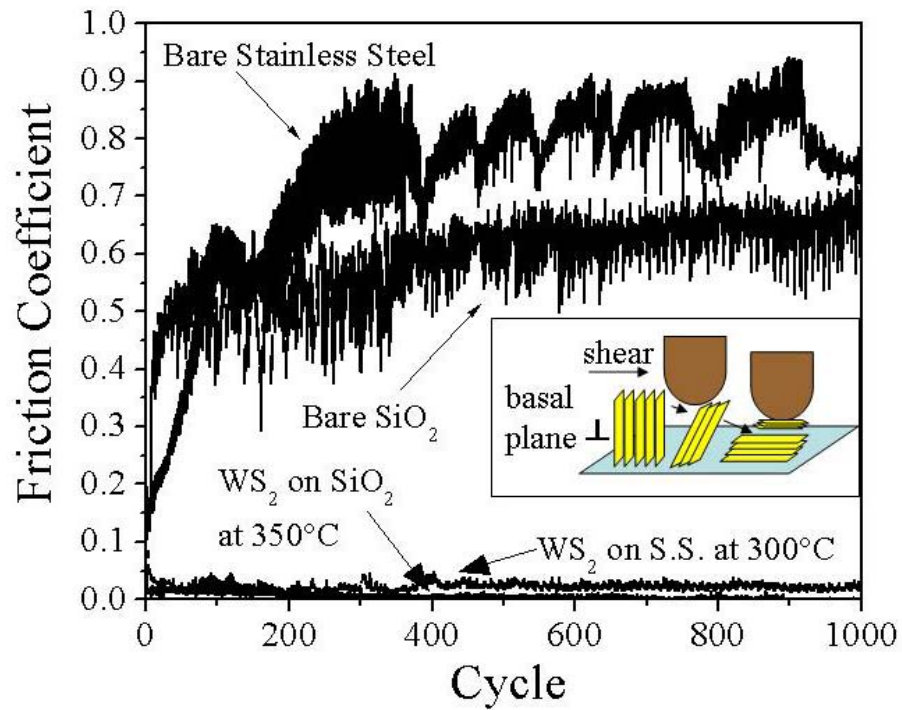


Fig. 3.5. Friction coefficient measurements of ALD grown WS₂ on stainless steel and SiO₂ substrates at 0.8 GPa contact stress in dry nitrogen. Referenced friction coefficients of bare substrates are shown for comparison. Inset shows shear-induced reorientation and transfer film formation for perpendicular basal planes (350°C WS₂ film on SiO₂).

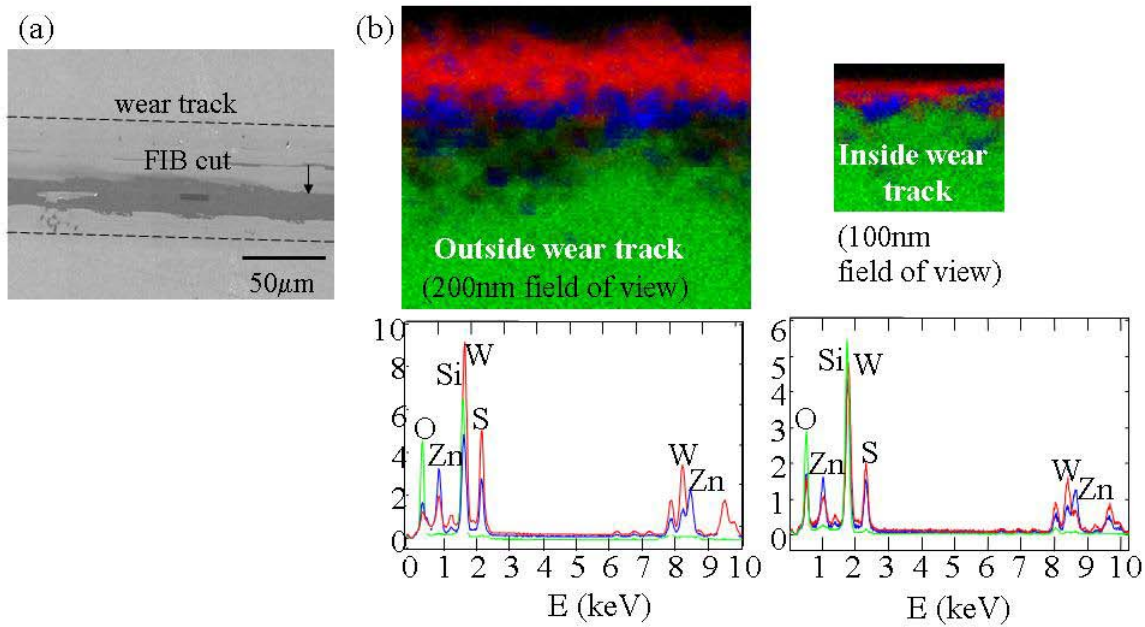


Fig. 3.6. (a) SEM image of ALD WS_2 on SiO_2 substrate grown at 300°C showing the wear track from test in Fig. 5, and location of where the FIB-cut was taken inside the wear track. (b) Cross-sectional TEM/X-ray spectral image maps inside and outside wear track with corresponding elemental X-ray peaks of constituents present (green= SiO_2 , blue= Zn , and red= WS_2). Both pictures are on the same scale.

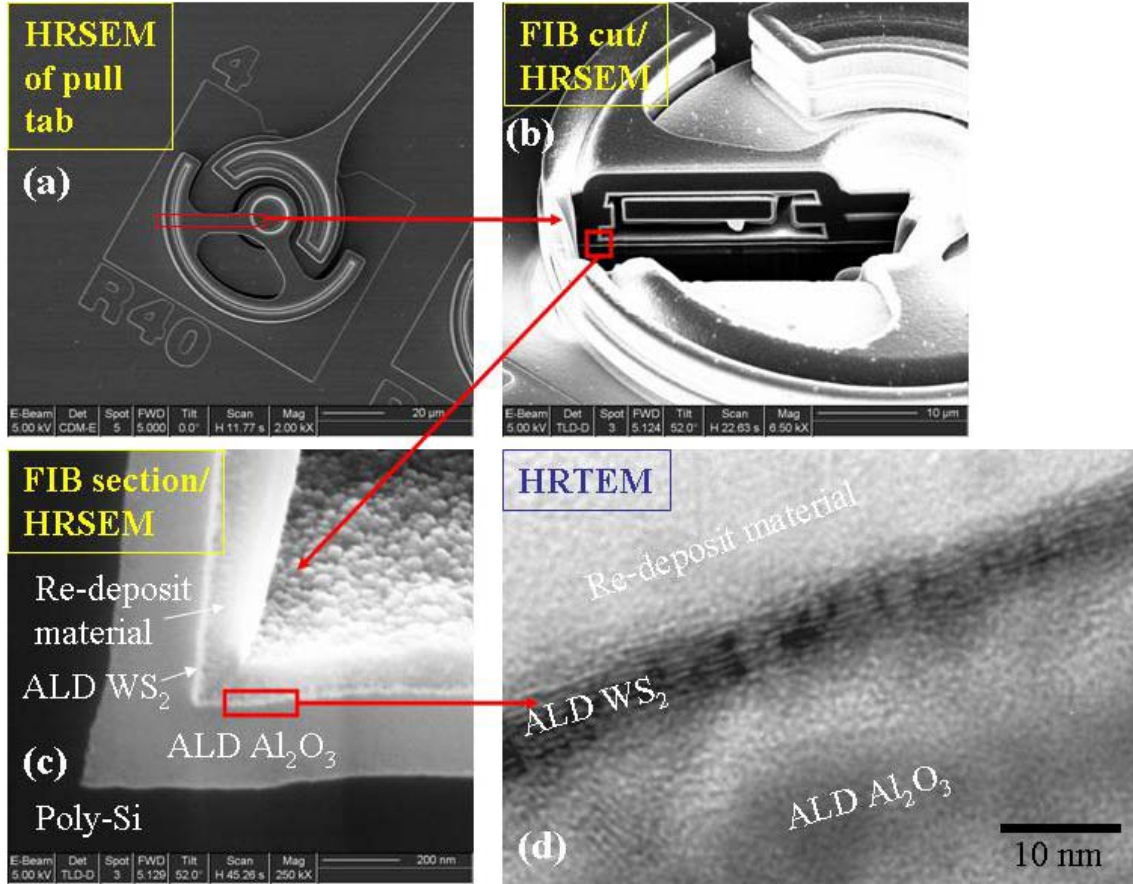


Fig. 3.7. (a-c) SEM and (d) TEM images of FIB-cut made on ALD WS_2/Al_2O_3 stack deposited on MEMS pull tab test structure showing the conformal growth on high aspect ratio, buried and shadowed surfaces.

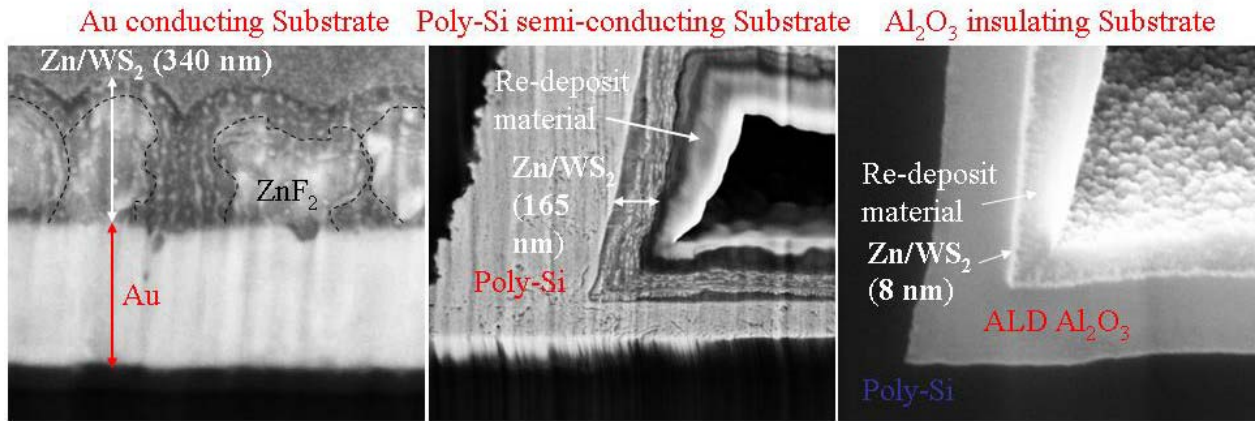
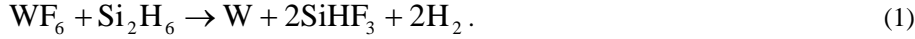


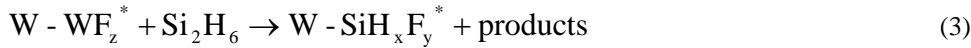
Fig.3.8. SEM images of FIB-cuts made on MEMS pull tab test structure showing the affects of (a) HF-byproduct from WS₂ reaction vapor etching the poly-Si and (b) ALD Al₂O₃ film protecting against HF attack.

4. GROWTH AND CHARACTERIZATION OF W AND W/AL₂O₃ LAMINATES

Nanolaminate films consisting of tungsten and alumina bilayers were grown at 125°C using atomic layer deposition (ALD). The ALD deposition of tungsten was accomplished by alternating exposures of WF₆ (99.9+%, Aldrich) and Si₂H₆ (99.998+%, Voltaix). The chemical vapor deposition (CVD) reaction for tungsten growth is given by [1],



The tungsten ALD reaction splits Eqn. 1 into two half reactions which are given by [2-4],

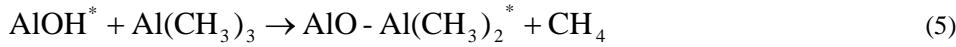


where the asterisks represent the surface species, and the stoichiometry of the surface species are left undefined to allow for different possible surface reactions. The successive application of reactions 2-3 at 125°C in an alternating sequence leads to tungsten deposition. Tungsten ALD on alumina proceeded through a 10 cycle nucleation period during which $24 \pm 1 \text{ \AA}$ of tungsten are deposited, followed by steady-state growth rate of $4.1 \pm 0.1 \text{ \AA/cycle}$.

Alumina (Al₂O₃) ALD deposition was performed by alternating exposures of water and trimethylaluminum. The CVD reaction for alumina deposition is given by [5],



The alumina ALD reaction splits Eqn. 4 into the following half reactions[5],



where the asterisks indicate the surface species. Sequential applications of reactions 5-6 leads to alumina deposition. Alumina ALD on tungsten nucleated within the 1st cycle, and the film thickness grew at $1.2 \pm 0.1 \text{ \AA/cycle}$.

The ALD reactions were carried out in a viscous flow reactor. An ultra high purity nitrogen carrier gas (UHP N₂, Airgas) was maintained at a pressure of 1 Torr using a flow rate of 200 SCCM. During tungsten growth, the WF₆ and Si₂H₆ were alternately pulsed into the nitrogen carrier flow using computer controlled gas switching valves. The Si₂H₆ was dosed for 10 seconds followed by a 25 second purge, then the WF₆ was dosed for 4 seconds followed by another 25 second purge. This pulse sequence was repeated until the desired tungsten film thickness was reached. After the last tungsten cycle the alumina film was grown by a 2 second TMA dose followed by a 20 second purge, then a 2 second water dose followed by another 20 second purge. This pulse sequence was repeated until the desired film thickness had been obtained.

For this study, two sets of nanolaminate films were grown on silicon and sapphire substrates. One set of nanolaminates had a total film thickness of 500 Å and films were grown which were composed of 2, 4, and 8 bilayers. The second set of nanolaminates had a total thickness of 1000 Å with films composed of 4, 8, and 16 bilayers. A TEM cross section of a representative nanolaminate film is shown in Fig.1 All surfaces were initially coated with 40 cycles (~48 Å) of alumina to provide an adhesion layer. Nanolaminate films were grown on the alumina adhesion layer by alternating tungsten and alumina deposition. For every film grown in this study, the alumina layer thickness in the bilayers was kept constant at 48 Å and the tungsten thickness was varied in order to achieve the desired total thickness.

Nucleation phenomena during atomic layer deposition (ALD) can critically affect the growth of nanolaminates. One example is W/Al₂O₃ nanolaminates where the nucleation of W on Al₂O₃ limits the minimum achievable thickness of a continuous and ultrasmooth W nanolayer to ~25Å. Quartz crystal microbalance (QCM) studies can measure the mass gain per cycle (MGPC) during ALD. QCM investigations of W ALD nucleation on Al₂O₃ reveal complex behavior. Figure 2 shows the QCM data during the first 30 cycles of ALD W growth on Al₂O₃. Clearly the growth begins very slowly and then begins to accelerate around the 5th cycle.

The MGPC data in Figure 2 reveals that WF_6 exposures lead to little mass gain for the first 4 cycles. After 5 cycles, the MGPC increases and reaches a maximum after 12 cycles. A "ringing" behavior is clearly observed for the MGPC for WF_6 and a second maximum is observed before reaching the steady state W ALD growth rate. Figure 2 also shows the MGPC for a W film which is clearly correlated with the evolution of surface roughness. The growth of W islands is also revealed by atomic force microscope measurements of RMS roughness, shown in Fig. 3. Modeling of these QCM results is in agreement with three-dimensional W island growth that produces a maximum in the MGPC which corresponds to the largest W surface area prior to the coalescence of the W islands, as shown in Fig. 4. The maximum roughness is observed after 9 cycles as the W islands are reaching their largest surface area prior to coalescence. The ratio of the WF_6 and Si_2H_6 MGPCs shown in Fig. 1b also changes and reveals distinct growth regimes (separated by the vertical line) that suggest that the relative density of reactive surface sites evolves as W islands are created, grow, and coalesce prior to forming a continuous W film.

In contrast, Al_2O_3 nucleates rapidly on W films. Figure 3(a) shows the QCM data during the first 15 cycles of Al_2O_3 growth on ALD W; the corresponding pressures measured during the growth are shown in 3(b). From the QCM data it is clear that a very large mass gain is observed during the first ALD cycle. The inset in 3(c) shows the QCM data for a single Al_2O_3 cycle during steady state growth behavior superimposed on the pressure measured in the reactor during this cycle. The mass gain per cycle during the TMA exposure is indicated by m_{TMA} and the mass gain per cycle during the water exposure is indicated by m_{H_2O} .

References

- [1] T. Kodas and M. Hampden-Smith, *The Chemistry of Metal CVD*, Weinheim, New York, (1994).
- [2] J. W. Klaus, S. J. Ferro, and S. M. George, *Thin Solid Film* **360**, (2000), pg. 145.
- [3] J. W. Klaus, S. J. Ferro, and S. M. George, *Appl. Surf. Sci.* **162-163**, (2000), pg. 479.
- [4] J. W. Elam, C. E. Nelson, R. K. Grubbs, and S. M. George, *Thin Solid Films* **386**, (2001), pg. 41.
- [5] A. W. Ott, J. W. Klaus, J. M. Johnson, and S. M. George, *Thin Solid Films* **292**, (1997), pg. 135.

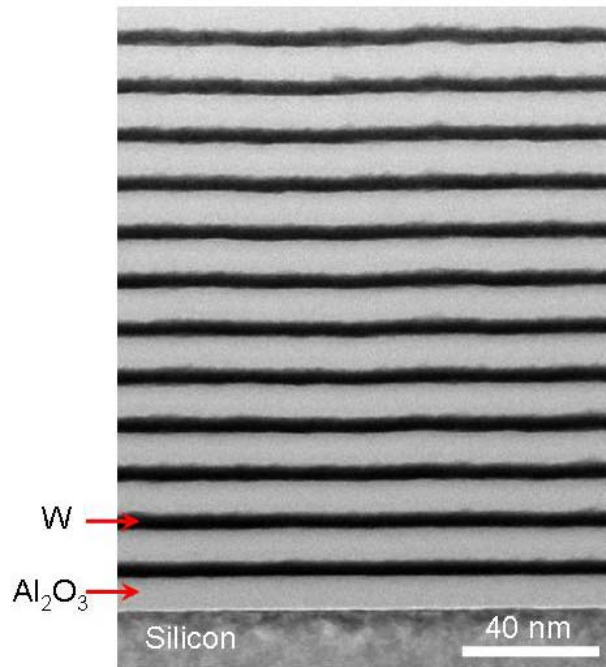


Fig. 4.1 12-layer W/Al₂O₃ nanolaminate structure deposited on a Si substrate by ALD

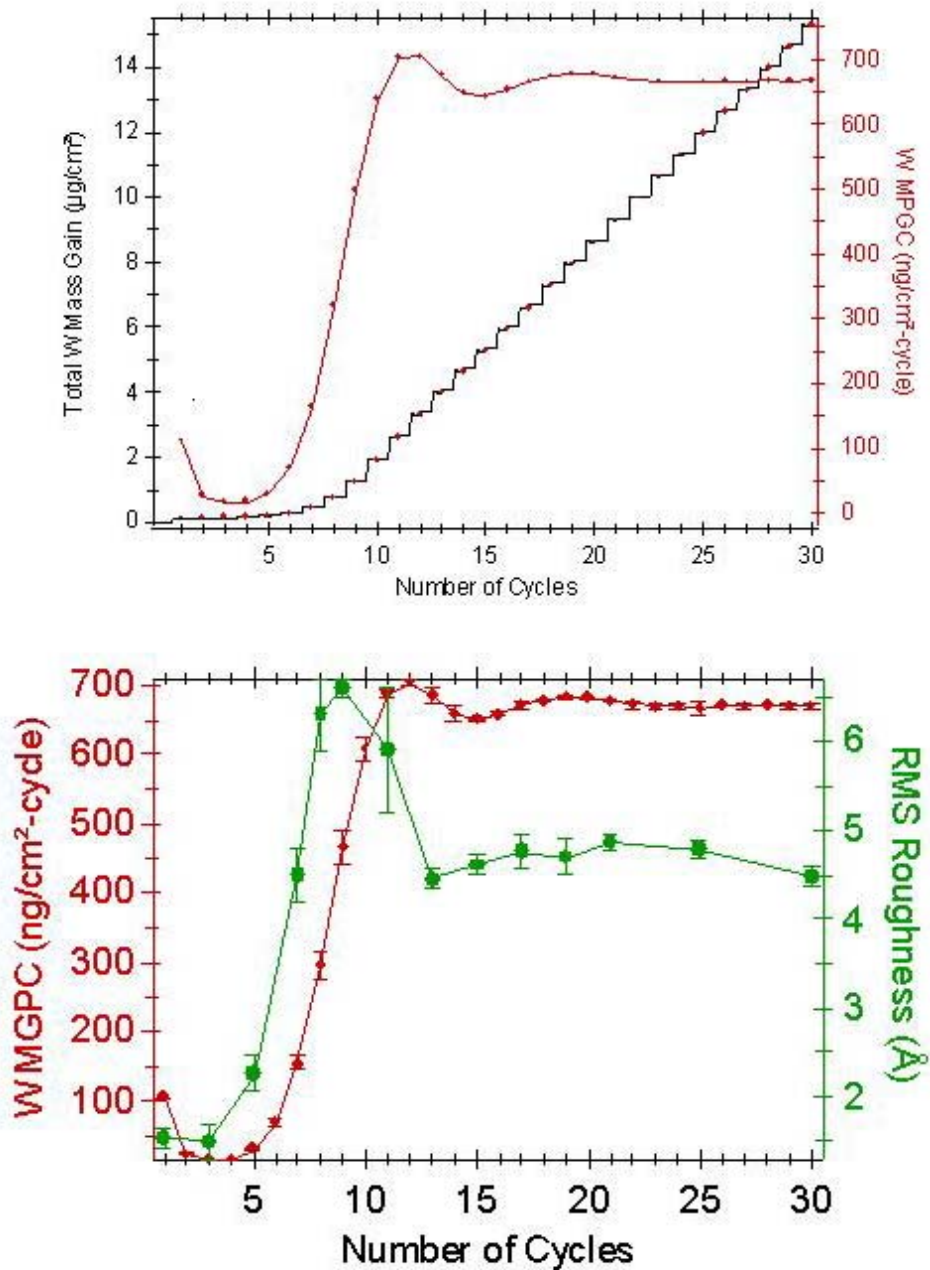


Fig. 4.2 Nucleation phenomena in W/Al₂O₃. Top: quartz crystal microbalance measure of total mass gain and W mass gain per cycle (WMGPC). Bottom: WMGPC and rms surface roughness during nucleation.

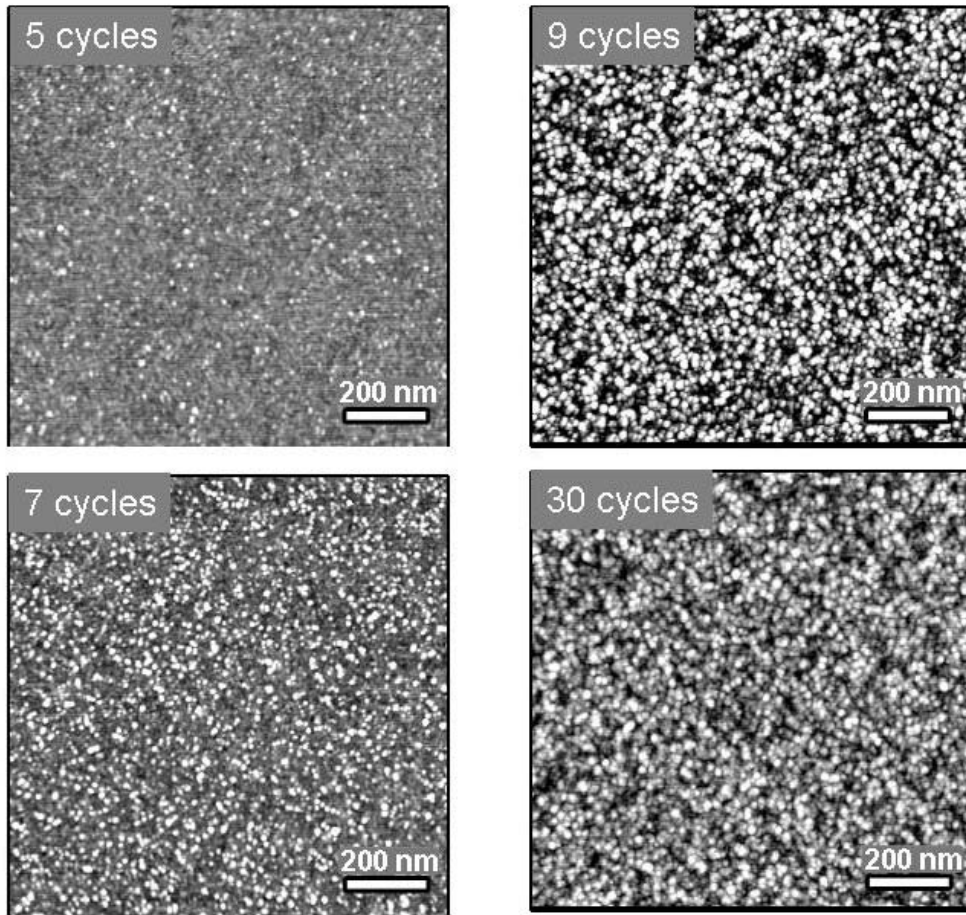


Fig. 4.3 AFM images of W nuclei on Al₂O₃ at different points in the nucleation process.

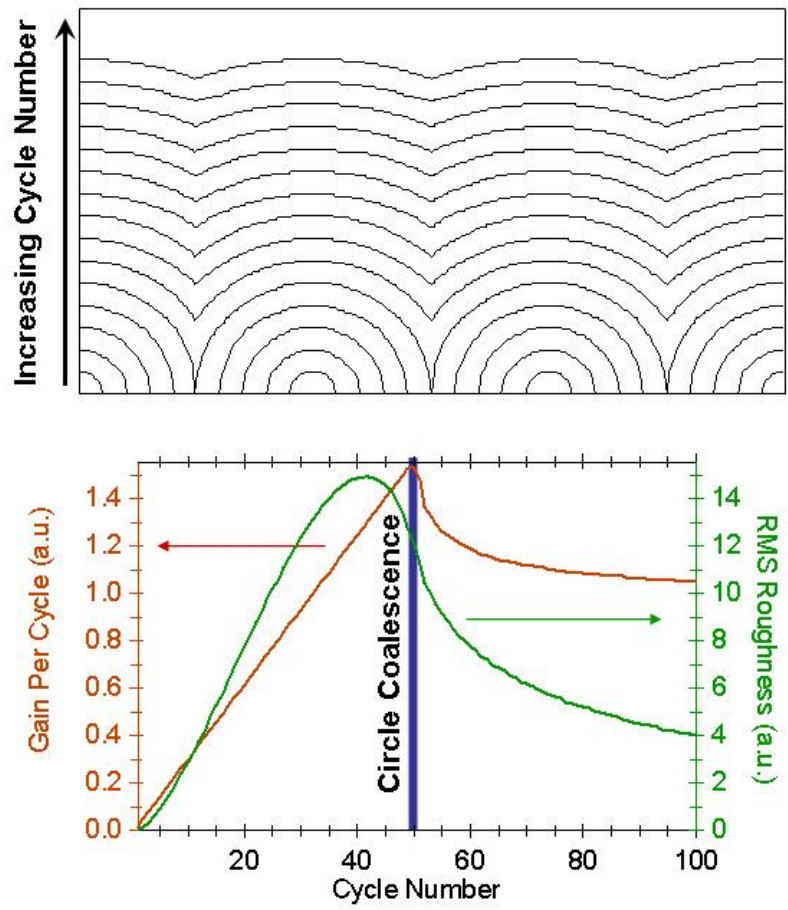


Fig. 4.4 Hemispherical cap model of nucleation and coalescence and qualitative predicted WMGPC and rms surface roughness characteristic of the model.

5. FRACTURE OF ATOMIC LAYER DEPOSITED TUNGSTEN FILMS

Low friction and good wear resistance are important factors controlling the performance and reliability of silicon based MEMS and nickel based LIGA structures. While adequate for some applications, as-produced material properties severely restrict use of these structures in many dynamic applications. In addition, the severe geometric constraints of many micromechanical systems and the need to avoid stress gradients make most deposition methods for applying performance enhancing friction and wear-resistance coatings impossible. Atomic layer deposition (ALD) is ideally suited for applying films on high aspect ratio MEMS and LIGA structures. ALD is a chemical vapor deposition process using sequential exposure of reagents with a self-limiting surface chemistry. (Ritala and Leskela [1]) The self-limiting chemistry results in conformal coating of high aspect ratio structures with monolayer precision.

ALD tungsten films are of particular interest for use as MEMS and LIGA coatings due to their high hardness and good wear resistance. However, measurement of mechanical and tribological properties and in particular film resistance to deadhesion presents a significant challenge as most conventional test methods are difficult to apply to very thin films. As a consequence, property data is extremely limited. We have therefore begun a study of ALD tungsten film on silicon substrate properties using nanoindentation techniques to determine mechanical behavior and nanoscratch techniques to measure fracture resistance at small loads characteristic of microsystem operation.

The tungsten films used in this study were deposited using atomic layer deposition at 300°C onto polished silicon substrates to thicknesses of 1, 5, 10, 50, and 200 nm. A native surface oxide covered the substrate surfaces. The films were nanocrystalline and with a gradient in density that ranged from 80 percent of theoretical value along the substrate interface to full density for thicknesses greater than 4 nm. The range of thicknesses served to highlight the evolution of film and substrate contributions to strength and adhesion.

Nanoindentation was used to determine elastic modulus and hardness values of these films as a function of contact depth using continuous stiffness with a DCM head and 50 nm radius Berkovich diamond indenter on a Nano Indenter XP™. Continuous stiffness was run at 45 Hz at displacement amplitudes of 1 and 2 nm. Nanoscratch tests using a 1 μm radius conical indenter tip were then conducted to determine the scratch resistance for the films. The tests were conducted by simultaneously driving the indenter into the films at a loading rate of 500 N/s and across the films at a lateral displacement rate of 0.5 m/s to a maximum load of 100 mN. During each test, the normal and tangential loads and the scratch distance were continuously recorded. The resulting scratch tracks were then examined using optical and scanning electron microscopy.

Mechanical Properties

Nanoindentation showed that elastic modulus and hardness increased with film thickness. The results are shown in Figure 1 where modulus and hardness values are plotted as a function of contact depth. Also shown for comparison are values for sputter deposited tungsten and the mirror polished silicon substrate. For films up to 10 nm thick, the measured moduli tracked substrate values. Values for thicker films were significantly higher than those of the substrate, with the thickest film values exhibiting little substrate influence. Nevertheless, the elastic modulus values were significantly lower than corresponding sputter deposited tungsten films. (Cordill et al. [13]) Hardness of the tungsten films also increased significantly with film thickness. (Figure 1b) However, the near surface decrease in values masks actual property behavior for the thinnest films. Hardness of the thickest film equaled values for sputter deposited films, thereby achieving a primary goal for using this film system.

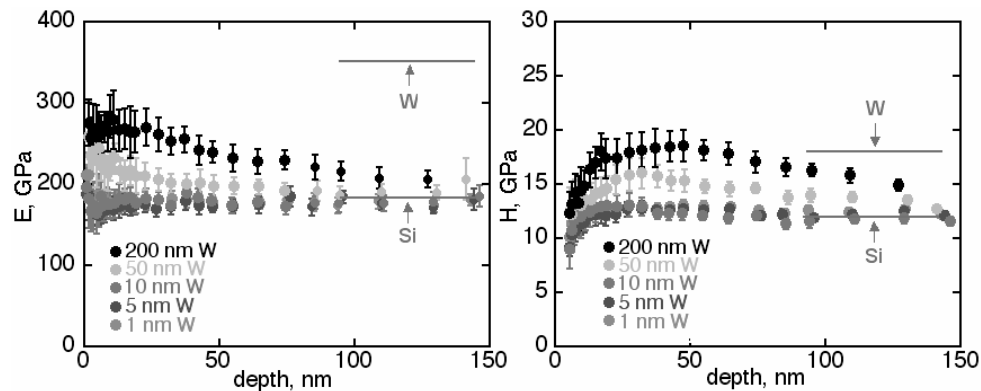


Figure 5.1. (a) Elastic modulus and (b) hardness increased with film thickness. The values were higher than those of the silicon substrate. Bulk tungsten and silicon substrate values are shown for comparison.

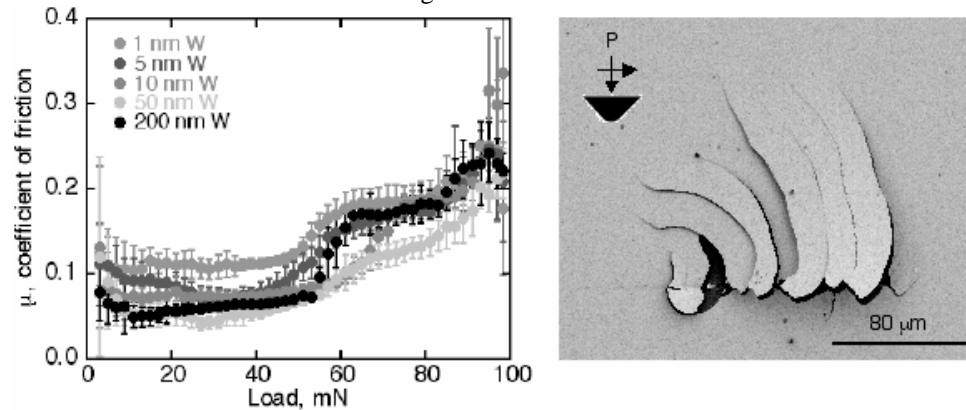


Figure 5.2. Nanoscratch tests using a conical indenter show that (a) frictional response varied with film thickness. (b) At loads near 50 mN, these tests triggered channel cracking and delamination as shown for the 200 nm thick ALD tungsten film.

Scratch Tests

A series of nanoscratch tests were conducted on all samples to determine scratch resistance. These tests showed a strong surface effect and marked increase in frictional forces at loads exceeding 40 mN. (Figure 2a) For the 200 nm film, the increase in friction corresponded to extensive channel cracking and delamination. (Figure 2b) The channel cracks initiated at the edge of the scratch track and followed a semi-circular path away from the track eventually becoming parallel to the scratch track. The cracks formed in succession parallel to the path of previous cracks. These cracks were stable and limited in length.

Close examination of scratch tracks strongly suggests that fracture began by film delamination forming circular debonded regions. The channel cracks grew along a path defined by the outer boundary of these debonded regions. The limit of channel crack growth back along a path parallel to the scratch track also appears to correspond to the size of the initial debonded region. Subsequent channel cracks grew along paths parallel to the initial channel crack at a nearly uniform spacing of 19 μm when measured away from the scratch track. A series of scratch tests sampling all orientations shows the same pattern of cracking, the same uniform crack spacing, and initial circular film delamination in all tests.

Discussion

Thermal mismatch between the films and native oxide substrate surface layers created by cooling from 300°C to ambient temperatures led to in-plane residual tensile stresses of 400 MPa determined from corresponding coefficients of thermal expansion. These stresses provided the stored strain energy for film fracture and delamination.

Film Fracture

Several studies have derived solutions for film and interfacial fracture energies where residual tensile stresses dominate fracture behavior. (Beuth [2]; Beuth and Klingbell [3]; Hu et al. [4]; Hutchinson and Suo [5]; Nakamura and Kamath [6]; Thouless, Cao, and Mataga [7]; Thouless [8]; Thouless, Olsson, and Gupta [9]; Vlassak [10]; Xia and Hutchinson [11]; Ye et al. [12];) These analyses are based on the assumptions that the film and substrate are elastic isotropic solids with dissimilar elastic moduli, the film is subject to a uniform, equibiaxial in-plane tensile stress, and the film thickness is much less than the substrate thickness. When the steady state strain energy release rate is greater than the critical strain energy release for film fracture, crack channeling occurs across the film.

For a through-thickness single channel crack forming in a residually stressed film, the mode I steady state strain energy release rate at fracture, $\Gamma_{I,ss}$, is given by, (Hu et al. [4]; Thouless [8]; Beuth [2]; Hutchinson and Suo [5]),

$$\Gamma_{I,ss} = \sigma^2 h (1 - \nu_f^2) \pi g(\alpha, \beta) / 2E_f \quad (1)$$

In this equation, σ is the stress in the film, h is the film thickness, E_f is the elastic modulus of the film, ν_f Poissons ratio for the film, and $g(\alpha, \beta)$ is nondimensionalized integral of the crack opening displacement. (Beuth [2]) The analysis was extended to multiple crack systems to account for crack interaction effects on strain energy release rates and is a function of crack spacing and film thickness. (Thouless [8]; Thouless, Olsson, Gupta [9]; and Hutchinson and Suo [5]). The large spacing to film thickness ratio exhibited by the ALD tungsten film channel cracks show interaction effects are insignificant and eqn (1) therefore defines the film fracture energy. For ALD tungsten on a native silicon dioxide surface layer where $\nu_f = 0.6$ and $\nu_s = 0.07$, $g(\alpha, \beta)$ is equal to 2.3117. This gives a mode I steady state release rate of 0.4 J/m². The corresponding fracture toughness of the film is 0.34 MPa-m^{1/2}.

Delamination

When the fracture energy of the interface is substantially less than the toughness of the film and substrate, channel cracking can trigger interfacial failure. Ye et al. [12] have shown that the mixed mode interfacial strain energy release rate, Γ_i , under these conditions is given by,

$$\Gamma_i = \omega_i \sigma^2 h (1 - \nu_f^2) / E_f \quad (2)$$

where ω_i is a dimensionless prefactor depending on α and β . Their finite element calculations provided the following approximation for ω_i ,

$$\omega_i = \frac{1}{2} \left(\frac{\eta_i}{1 + \eta_i} \right)^{1-2s} \left[1 + \lambda_3 \exp(-\lambda_4 \sqrt{\eta_i}) \right] \quad (3)$$

With $\eta_i = a/h$, $s = 0.654$, $\lambda_3 = 0.796$, $\lambda_4 = 0.694$, and 'a' equal to the delamination half width, ω_i is equal to 0.5 which is typical for stiff films on compliant substrates. (Drory et al. [13]) The interfacial fracture energy is then equal to 50

mJ/m^2 . This value is composed of normal mode I and shear mode II contributions with mode I contribution given by the following,

$$\Gamma_I = \Gamma \sqrt{1 + \tan^2 \left\{ (1 - \lambda) \psi \right\}} \quad (4)$$

With a phase angle of loading, ψ , equal to 60° and the material constant, λ , equal to 0.3, the corresponding mode I fracture energy is 30 mJ/m^2 . This value is less than the range of mode I values, 0.1 to 0.5 J/m^2 , observed for sputter deposited tungsten films on silicon substrates. (Cordill et al. [14]) They are also somewhat lower than film adhesion values measured for CVD films. However, a mode I value of 30 mJ/m^2 may accurately reflect the influence of lower film density along the substrate interface.

Conclusions

We have conducted a systematic study of the mechanical property and fracture behavior of atomic layer deposited tungsten films as a function of film thickness. These films were deposited at 300°C creating a state of high residual tensile stress. Nanoindentation testing showed that elastic modulus and hardness increased with film thickness. For the thickest films, these values were substantially higher than the substrate values with the hardness equaling values for bulk and sputter deposited films. Nanoscratch tests were then used to study scratch adhesion. These tests triggered channel cracking and delamination in the thickest film. The cracks formed in succession parallel to the path of previous cracks. Corresponding film and interfacial fracture energies were determined using mechanics-based channel cracking and delamination models. For our film system, the analysis showed that film fracture occurred at an energy of 0.4 J/m^2 . The corresponding interfacial fracture energy for film delamination between the channel cracks was 50 mJ/m^2 with a mode I component equal to 30 mJ/m^2 . This value is less than the work of adhesion for sputter deposited tungsten films on silicon substrates but may accurately reflect the influence of lower film density along the substrate interface.

References

- [1] Ritala, M., Leskela, M., Atomic Layer Deposition, in Handbook of Thin Films, Nalwa, H. S., ed., ch. 2, vol. 1, Academic Press, San Diego, CA (2001).
- [2] Beuth, J. L. Jr., Cracking of thin bonded films in residual tension, *Int. J. Solids Structures*, 29, 1657-1675 (1992).
- [3] Beuth, J. L., Klingbeil, N. W., Cracking of thin films bonded to elastic-plastic substrates, *J. Mech. Phys. Solids*, 44, 1411-1428 (1996).
- [4] Hu, M. S., Evans, A. G., The cracking and decohesion of thin films on ductile substrates, *Acta metal.*, 37, 917-925 (1989).
- [5] Hutchinson, J. W., Suo, Z., Mixed mode cracking in layered materials, *Advances in Applied Mechanics*, 29, 63-191 (1992)
- [6] Nakamura, T., Kamath, S. M., Three-dimensional effects in thin film fracture mechanics, *Mechanics of Materials*, 13, 67-77 (1992).
- [7] Thouless, M. D., Cao, H. C., Mataga, P. A., Delamination from surface cracks in composite materials, *J. Materials Science*, 24, 1406-1412 (1989).
- [8] Thouless, M. D., Crack spacing in brittle films on elastic substrates, *J. Am. Ceram. Soc.*, 73, 2144-2146 (1990).
- [9] Thouless, M. D., Olsson, E., Gupta, A., Cracking of brittle films on elastic substrates, *Acta metal. mater.*, 40, 1287-1292 (1992).

- [10] Vlassak, J. J., Channel cracking in thin films on substrates of finite thickness, *Int. J. Fracture*, 119/120, 299-323 (2003).
- [11] Xia, Z. C., Hutchinson, J. W., Crack patterns in thin films, *J. Mech. Phys. Solids*, 48, 1107-1131 (2000).
- [12] Ye, T., Suo, Z., Evans, A. G., Thin film cracking and the roles of substrate and interface, *Int. J. Solids Structures*, 29, 2639-2648 (1992).
- [13] Cordill, M. J., Bahr, D. F., Moody, N. R., Gerberich, W. W., Recent developments in thin film adhesion measurement, submitted to *IEEE Transactions on Device and Materials Reliability* (2004).
- [14] Drory, M. D., Thouless, M. D., Evans, A. G., On the decohesion of residually stressed thin films, *Acta metal.*, 36, 2019-2028 (1988).

6. PROPERTIES AND FRACTURE OF TUNGSTEN-ALUMINA ATOMIC LAYER DEPOSITED NANOLAMINATES

In many current microelectromechanical systems (MEMS) and microelectronic devices, coatings are often applied to improve component lifetime and performance. Ideally, these coatings should have both low frictional coefficients in order to minimize lateral forces and a high hardness to decrease permanent damage and wear. Limited success has been achieved by combining individual coatings that exhibit either a desirable frictional coefficient or desirable wear resistance. Ideally, a single robust coating would both increase the wear resistance and decrease the friction coefficient. In addition to meeting these requirements, it is critically important that the coating have both high fracture toughness and substrate adhesion. Although deposition techniques currently exist which may be used to create candidate planar films, atomic layer deposition (ALD) represents an ideal technique for the deposition of wear resistant coatings in complex geometry devices such as MEMS.

ALD is a modified chemical vapor deposition process where the reaction pathways are split into chemical half-reactions. These half-reactions are self-limiting at the sample surface, where saturation of available surface sites limits the adsorption, and consequent growth, of the reactive species. Through sequential exposures of half-reactions, a film may be grown to any given thickness. As a direct result of the self-limiting surface reactions, ALD is both a highly controllable and conformal film deposition technique with documented depositions occurring with submonolayer growth control and uniform film deposition over features with aspect ratios in excess of 100:1 (Mayer et al. [1]). ALD nanolaminates are of particular interest as they offer the unique ability to engineer both the laminate chemistry (with respect to the individual laminate layers) and sample structure (with respect to the individual layer thickness).

As early as 1970, Koehler had proposed that by modifying both layer thickness and the ratio of shear moduli, it would be possible to design strong microstructures (Koehler [2]). Indeed, multiple research groups have observed that nanolaminated microstructures do display a functional relationship showing increasing hardness with decreasing layer spacing (Xhang et al. [3]; Chu and Barnett [4]; Misra et al. [5]). There have been several attempts to model this hardening response in laminated structures using both Hall-Petch scaling relations as well as independent energy-based designs; however, the models tend to diverge from experimental results at very small length scales (Freidman [6]; G-Berasategui et al. [7]). It has also been observed that increased wear resistance is directly related to the bilayer thickness with increasing resistance at smaller thickness (Ruff and Lashmore [8]). Additionally, *in-situ* TEM observations of crack bridging in nanolaminates imply that these structures could display increased fracture toughness compared to single component blanket films (Kramer and Foecke [9]). Interestingly, Koehler predicted that increasing the difference in the shear moduli of the layers would increase the hardness of the system, yet the majority of published literature deals with metal-metal or ceramic-ceramic laminate structures where the shear moduli are similar. In the current study, we have produced multilayers using nanocrystalline tungsten and amorphous aluminum oxide, where the difference in the shear moduli is approximately 77 GPa. Here we will look at the effect of nanolaminate structure on hardness, modulus and fracture toughness.

2 EXPERIMENTAL PROCEDURES

The ALD nanolaminates used in this study were deposited in a flow reactor at a temperature of 130 °C onto (0001) sapphire wafers. A 5 nm amorphous layer was present on the sapphire surface from mechanical polishing during processing. The ALD laminate samples were composed of alternating layers of amorphous aluminum oxide and nanocrystalline tungsten. For a more thorough description of this deposition process, refer to (Costescu et al. [10]). As a result of the low temperature growth, a density gradient develops during the first 4 nm of growth. As determined from x-ray reflectivity, in the alumina films this gradient ranges from 40 percent of fully dense alumina at 2 nm and plateaus at 80 percent density after 4 nm have been deposited. Similarly, the tungsten gradient shows 40-50 percent at 2 nm and plateaus between 80-90 percent of fully dense tungsten after 4 nm. The sample set was composed of 4, 8 and 16 bilayers of this alumina/tungsten series to a total composite film thickness of 100nm. In all the samples, the alumina layer was held constant at 4 nm and the metal layer was adjusted to fill the remaining volume as shown in Table 1.

Table 1. Set of nanolaminates used during testing.

# bilayers	Alumina Thickness (nm)	Tungsten Thickness (nm)	Volume Fraction - Alumina	Volume Fraction - Tungsten
4	4	21.1	15.9	84.1
8	4	8.4	32.3	67.7
16	4	2.1	65.6	34.4

Nanoindentation tests were used to determine the elastic modulus and indentation hardness of the nanolaminate films. All the indentation tests were performed using a MTS Nano Indenter® DCM operated using the continuous stiffness method (CSM) with a Berkovich diamond indenter tip. The CSM was operated at 70 Hz with a displacement amplitude of 2 nm. Ten separate indents were performed on each sample to ensure a representative behavior was obtained. To determine the scratch resistance of the laminate films, nanoscratch tests were performed using a MTS Nano Indenter® XP with both a berkovich and 1 μm radius conical tip. These tests were performed by

simultaneously applying a normal load at a rate of 250 N/sec and translating the stage at 0.5 μm/sec to a maximum normal load of 100 mN. The normal and tangential loads and displacements were continuously recorded during the entirety of the test. The resulting scratch tracks and film delaminations were examined using scanning electron microscopy.

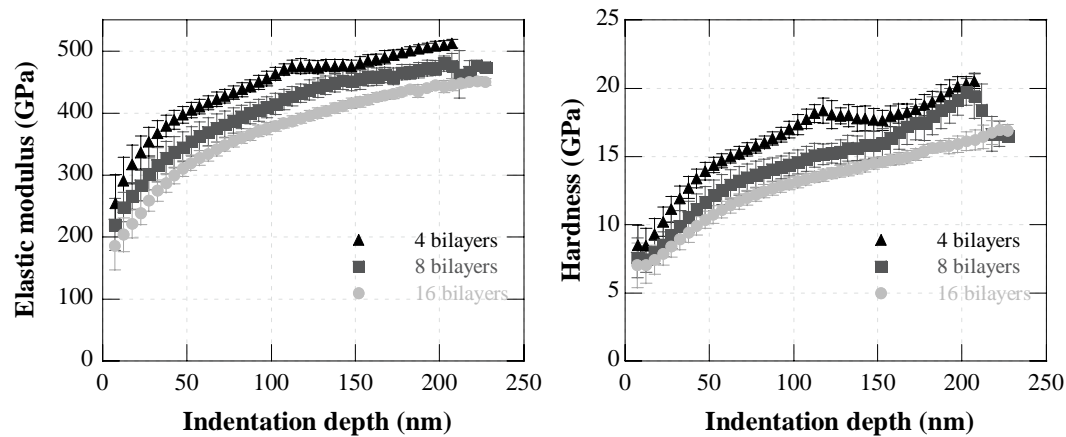


Figure 6.1. (a) Elastic modulus and (b) indentation hardness of the nanolaminate systems. The properties of bulk tungsten, alumina and sapphire are shown for comparison.

Results and discussion

Elastic Modulus and Hardness

The nanoindentation results show that the elastic modulus increased with decreasing number of bilayers. Previous experiments on blanket films of ALD tungsten and ALD alumina determined elastic modulus values of 280 and 145 GPa and hardnesses of 18 and 8 GPa, respectively (Moody et al. [11]). These values allow for a baseline approximation of laminate properties based on a simple rule-of-mixtures. As seen in Figure 1, the modulus for the laminates ranges from 183 GPa for the 16-bilayer sample to 248 GPa for the 4-bilayer composite at shallow displacements. These results compare well with what would be expected from a simple rule-of-mixtures approach. Since the total composite thickness is only 100 nm, a strong sapphire substrate effect quickly dominates properties; however by interpolating toward a zero penetration depth, approximations of the properties can be made. Similarly, the hardness response of the samples increased for decreasing numbers of bilayers, however values of 7.0 to 8.2 GPa are below what would be expected based on the simple rule of mixtures approach, possibly due to effects from the density gradient. Discontinuities were observed in all three samples on both the elastic modulus and hardness curves at large indentation depth. These events were seen as indentation displacement discontinuities during loading and most likely correspond to either fracture or delamination within the nanolaminate stack; however, scanning probe microscopy did not reveal any features other than plastic pileup around the indents.

Scratch Testing and Film Fracture

In order to determine the fracture resistance of the laminate films, nanoscratch tests using both 50 nm radius Berkovich and 1 μ m radius conical tips were performed. Representative images from these tests can be seen below in Figure 2, where it is immediately observed that for increasing number of bilayers the fracture toughness decreases. Additionally, the Berkovich tip generates increased channel crack formation compared to the spherical tip. It is hypothesized that this is due to the higher tangential stresses produced by the Berkovich tip. These higher tangential stresses result in a positive shift of the frictional coefficient, from 0.05 with a conical tip to slightly greater than 0.12 using the berkovich, an increase of almost a factor of 3.

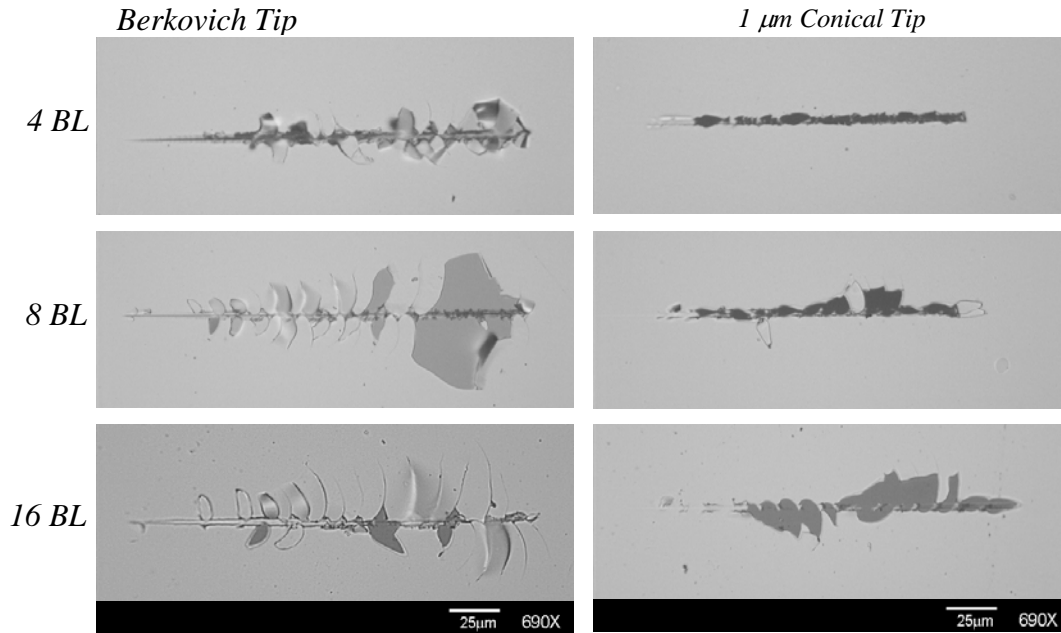


Figure 6.2. Scratch fracture and delaminations observed for both (a) Berkovich and (b) conical tips. The magnitude and extent of the fractures increases with decreasing layer period, and is noticeably larger for the Berkovich tip due to the increased lateral forces.

Unlike the results from single ALD tungsten films where scratch tests initiated extensive channel cracking and film debonding, there is no widespread delamination in the nanolaminate films. Rather, small channel cracks are localized near the scratch track and increase in magnitude as the normal and tangential loads increase. Interestingly, a strong reverse length scale is observed in the fracture behavior of the laminates. It can be seen that as the layer period decreases, the length of the channel cracks increase, contradicting the expected toughness results. One could argue that the toughness of the composite film is directly related to the total volume fraction of metal, where the metal acts to absorb energy plastically. Therefore, since the 16-bilayer system has a lower overall volume fraction of metal as compared to the 4- or 8-bilayer systems, the 16 bilayer system would have the lowest fracture toughness. Consequently, this argument would imply that a pure tungsten film would have the highest toughness when compared to the laminate films. However, this is in disagreement with previously observed results on ALD-W films (Moody et al. [11]). Nevertheless, these results imply that a maximum in the fracture toughness exists between the single blanket film of ALD-tungsten and the 4- bilayer laminated structure of ALD-tungsten and ALD-alumina.

Conclusions

We have initiated a study of atomic layer deposited nanolaminate-based composites using alternating layers of nanocrystalline tungsten and amorphous aluminum oxide. Using nanoindentation techniques, we have determined that the elastic modulus and hardness range for 4- 8- and 16-bilayer systems from 284 to 183 GPa and 8.2 to 7.0 GPa respectively at shallow displacements. From nanoscratch tests, a strong reverse length-scale affect was observed in the fracture behavior of the laminated films. It was seen that as the layer period decreased, the apparent toughness of the film decreased. When these results are compared to similar tests on blanket films of ALD-tungsten, a maximum in the fracture toughness can be predicted with bilayer thicknesses somewhat larger than 21nm of ALD-tungsten and 4 nm of ALD-alumina.

References

1. Mayer, T.M., Elam, J.W., George, S.M., Kotula, P.G. Goeke, R.S., Atomic-layer deposition of wear-resistant coatings for microelectromechanical devices, *Applied Physics Letters* 82, pp. 2883-2885 (2003).
2. Koehler, J.S Attempt to Design a Strong Solid, *Phys. Rev. B*, 2, pp. 547-551 (1970).
3. Xhang, X., Misra, A., Wang, H., Shen, T.D., Swadener, J.G., Embury, J.D., Kung, H., Hoagland, R.G., Nastasi, M., Strengthening mechanisms in nanostructured copper/304 stainless steel multilayers, *J. Mater. Res.* 18, pp. 1600-1606 (2003).
4. Chu, X., Barnett, S.A., Model of superlattice yield stress and hardness enhancements, *J. Appl. Phys.*, 77, pp.4403-4411 (1995).
5. Misra, A., Hirth, J.P., Kung, H., Single-dislocation based strengthening mechanisms in nanoscale metallic multilayers, *Phil. Mag. A*, 82, pp. 2935-2951 (2002).
6. Friedman, L.H., Towards a full analytic treatment of the Hall-Petch behavior in multilayers: Putting the pieces together, *Scripta Materialia*, 50 2, pp. 763-767 (2004).
7. G-Berasategui, E., Bull, S.J., Page, T.F., Mechanical Modeling of multilayer optical coatings, *Thin Solid Films*, 447-448, pp. 26-32 (2004).
8. Ruff, A.W., Lashmore, D.S., Effect of layer spacing on wear of Ni/Cu multilayer alloys, *Wear* 151, pp. 245-253 (1991).
9. Kramer, D.E., Foecke, T., Transmission electron microscopy observations of deformation and fracture in nanolaminated Cu-Ni thin films, *Phil. Mag. A*, 82, pp. 3375-3381 (2002).
10. Costescu, R.M., Cahill, D.G., Fabreguette, F.H., Sechrist, Z.A., George, S.M., Ultra-low thermal conductivity in W/Al₂O₃ Nanolaminates, *Science*, 303, pp. 989-990 (2004).
11. Moody, N.R., Jungk, J.M., Mayer, T.M., Wind, R.A., George, S.M., Gerberich, W.W., Fracture of atomic layer deposited tungsten films, submitted to Proceedings of ICF 11, Turin, Italy, (2005).

7. FINITE ELEMENT MODELING AND PROPERTIES OF ULTRA-THIN ALD FILMS

While finite-element modeling (FEM) has been applied to nanoindentation tests before, it has generally been used to more fully understand the indentation process to allow for further development of existing analytical models (Bhattacharya and Nix 1988; Bourcier et al. 1991; Laursen and Simo 1992); however, when existing analytical methods break down for very thin films (where a 10% rule is at the limit of nanoindenter instrumentation resolutions (Cai and Bangert 1995)), then FEM may be useful in separating the substrate response from the overall indentation curve. In general, the finite element method is based on slicing a representation of a sample into several pieces (elements), and connecting the pieces at specific nodes (where a node can be thought of as a pin that holds several elements together). Then when a stress is applied at some point on the structure, based on the constitutive equations of the system, a series of equations may be used to determine the equilibrium stresses on each element throughout the structure. As one can imagine, for even simple sample geometries with coarse meshes, the number of equations can quickly number in the thousands, making computation calculations necessary. For all the simulations presented here, ABAQUS/Standard version 6.3, a commercially available finite element simulation program, was used for the computer modeling with ABAQUS/CAE employed in post simulation modeling visualization. An overview of the simulation process is shown in Figure 6.1, from the generation of the sample mesh and indenter displacement command forming the simulation input file, to the processing of the simulation data using Excel VisualBasic macros.

Finite element modeling

A finite element simulation of an indentation test can be easily configured using a simple mesh (involving both the sample shape and the indenter tip geometry), material properties (of the sample and tip materials), and a specific indentation load or displacement function (to describe how the tip displaces into the mesh). For the case of an unknown film on a well-defined substrate, an iterative method may be used in which a series of simulations, with each simulation having a different set of properties for the unknown film is compared to actual indentation data. Then, by adjusting the properties of the unknown material so they more closely match with the experimental data, an approximation of the properties of an unknown film may be determined independent of any substrate contribution. For the procedure used here, the yield stress and elastic modulus of the unknown film are varied, while other parameters such as the work-hardening rate and Poisson's ratio are fixed at characteristic values (determined from the literature), as it has been observed that the simulations are not very sensitive to the work hardening rate but are very dependent on the yield stress and elastic modulus (Knapp et al. 1999).

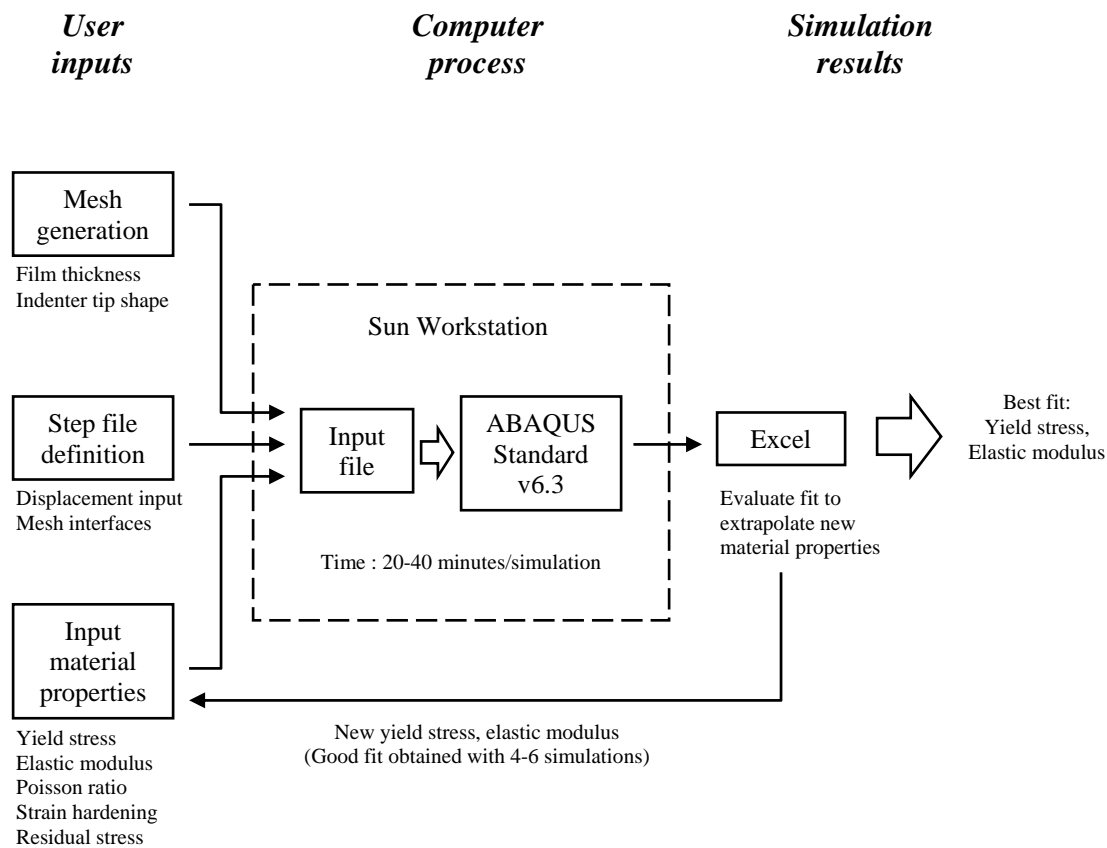


Figure 6.1. Flow chart of the modeling processes. Adapted from Knapp and coworkers (Knapp et al. 1999)

One of the more difficult tasks of running finite element simulations is the construction of a mesh that closely describes the sample geometry and indenter shape. This is especially important for shallow indentations, as tip blunting away from the ideal tip shape can yield large errors in the calculated properties. Therefore, both a precise determination of the layer thickness and description of the indenter tip shape are required for an accurate match between the simulation and the experimental data. While the ABAQUS software suite does include a meshing program, by necessity of the broad scope of the program the design is somewhat unwieldy and does not lend itself to minor modifications after mesh construction. Consequently, a specially designed Visual Basic mesh generator (designed at Sandia National Laboratories by James Knapp) was used to generate a two-dimensional FEM mesh with user specified layer thicknesses and indenter tip shape. In this generator, the tip shape is based on the contact area function of Equation 2.29 in order to account for the tip blunting at the indenter apex. The program produces a mesh file that describes the sample (composed of the film and substrate) and the indenter tip (Figure 6.2). It is important to note that while three-dimensional calculations would account for indenter tip asymmetry (as with Berkovich tips), it has been shown that the difference in the simulation solution only changes by a few percent, with greatly increased computational efficiency for the two-dimensional case (Knapp et al. 1997).

After a mesh is generated, the mechanical properties of the components in the mesh need to be defined. To accomplish this, all the materials are modeled as isotropic, elastic-plastic solids, where the plastic boundary is defined using a Mises yield criterion. An elastic modulus, yield stress, work hardening rate, density and Poisson's ratio are then assigned to the meshed film, substrate and indenter tip. For the diamond indenter tip, it is assumed that the tip is completely elastic with an elastic modulus of 1140 GPa and a Poisson's ratio of 0.07. Also, with amorphous and nonmetallic materials, the work hardening was assumed to be zero. The values for the substrate are determined from indentation tests and FEM modeling of the bulk substrate, using Poisson's ratio and work hardening rates based on literature values.

The final step is to define the interactions between the mesh surfaces and describe the indentation displacement profile (or loading history). For all the simulations discussed in this chapter, the film/substrate interface was

assumed to be perfectly bonded (i.e., no allowable interfacial slip or delamination). The sliding interaction between the indenter tip and the top surface was set for all simulations with a frictional coefficient of 0.2; however, it has been shown that there is no discernable effect on the overall simulation response when changing this coefficient from 0.0 to 1.0 (Knapp et al. 1999). Unlike nanoindentation tests, the finite element simulations were performed under displacement control, where the tip was displaced into the sample a certain distance and the mesh balanced the stresses based on the user specified material properties. The displacement experiment was modeled by a sequential series of loading steps (generally around 10 nm), followed by a short unloading (around 2 nm), until a maximum indentation depth was reached. From the unloading portion of the simulation, the stiffness (and consequently the reduced elastic modulus) was extracted as a function of depth using the same curve fitting methods as discussed for conventional nanoindentation data in Chapter 2.

A single simulation input file was then created by combining the user defined mesh, material properties and displacement files. This input file was then loaded into the ABAQUS software and allowed to run. After the simulation converges with the experimental data, a final simulation of a hypothetical “bulk” sample was done using the yield stress and elastic modulus from this best fit simulation, allowing for the determination of the hardness contribution of just the film (Follstaedt et al. 2004; Knapp et al. 1999).

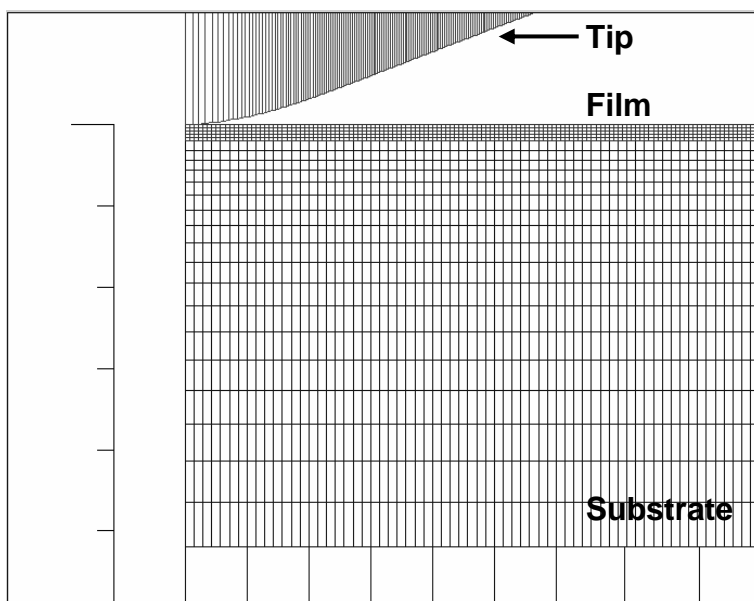


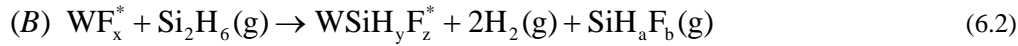
Figure 6.2. Example of 20 nm thin film mesh generated from Visual Basic macro.

Atomic layer deposition

Recently, a new deposition technique called atomic layer deposition (ALD) has gained prominence due to the unprecedented control it provides over film thickness, uniformity, density, and low roughness (Cameron et al. 2000; Ferguson et al. 2000; Klaus et al. 2000). ALD is essentially a modified chemical vapor deposition (CVD) process where the reaction pathway is separated into two separate half-reactions. In general, ALD deposition is described as a sequence of discrete, self-limiting, surface reactions where the absorption of the reactive species to the surface is the dominate process step (Sneh et al. 2002).

As binary CVD reactions can be easily separated into two half-reactions, ALD is generally applied to binary compounds such as oxides (Klaus et al. 1997), nitrides (Klaus et al. 1998), sulfides (Han et al. 1998), phosphides (Ishii et al. 1997) and metal alloys (Klaus et al. 2000); however, the use of single elements has also been reported

(Klaus et al. 2000). The main requirement of ALD is that the half-reactions are self-limiting at the substrate surface. Given this, each half-reaction goes to completion at the surface, and then stops until the next half-reaction is initiated. This is generally described as *A-B* growth where *A* and *B* represent each successful half-reaction during the deposition. An example of this *A-B* layering for the deposition of tungsten is shown in Equations 6.1 and 6.2 (Costescu et al. 2004),



In these reactions, the asterisks indicate the active surface species and the stoichiometry is kept indefinite as there are several reaction pathways. $\text{Si}_2\text{H}_6(\text{g})$ is used to reduce the WF_x^* species to metallic tungsten by stripping the fluorine and forming volatile gases (Klaus et al. 2000). By repeating this *A-B* layering, the film thickness can be increased with a high degree of accuracy. Since film growth occurs at the sample surface, ALD is a highly conformal technique.

Results

Substrate calibration

In order to run the finite element simulations, an accurate indentation calibration of the substrate elastic modulus and yield stress were required. From indentation tests using bare silicon, the applied load and contact stiffness were determined as a function of indenter displacement (Figure 6.4). Then, using the method outlined above, finite element simulations with varying elastic modulus and yield stress values were performed to obtain a best-fit with this experimental data. For all simulations, the silicon density was set at 2.33 g/cm^3 and the Poisson's ratio was 0.223 (Callister 1997). Using these values and iterating the modulus and yield stress, it was seen that the model converged when $E = 172.5 \pm 5.4 \text{ GPa}$ and $\sigma_{ys} = 5.4 \pm 0.9 \text{ GPa}$, resulting in an indentation hardness of, $H = 12.6 \pm 1.2 \text{ GPa}$ (Figure 6.5), which is in good agreement with previously published values (Knapp and Follstaedt 2004).

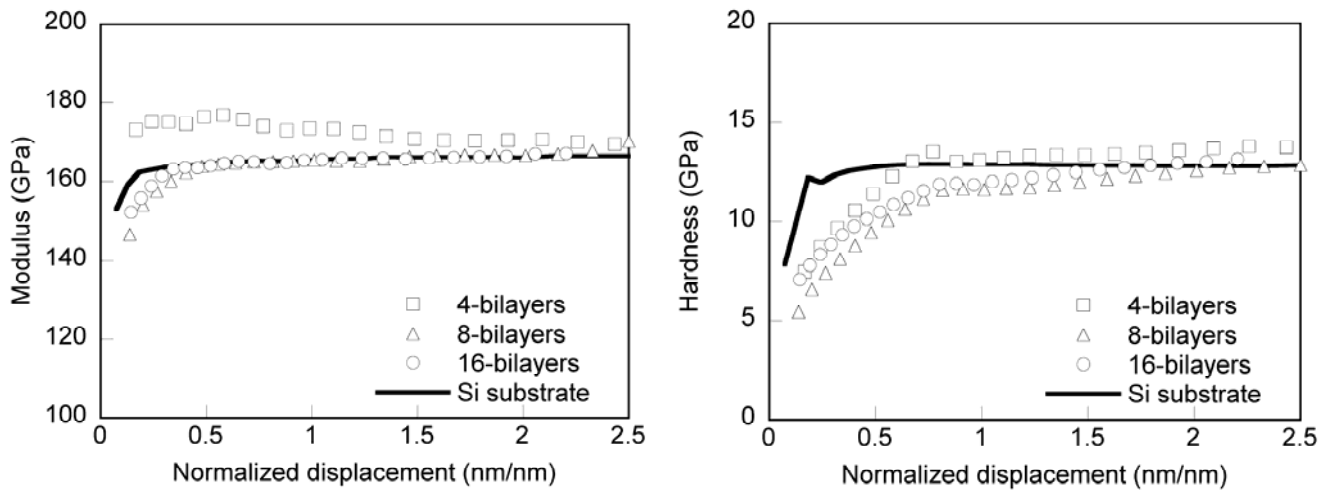


Figure 6.4. Normalized modulus and hardness for nanolaminate indentation tests on silicon substrate.

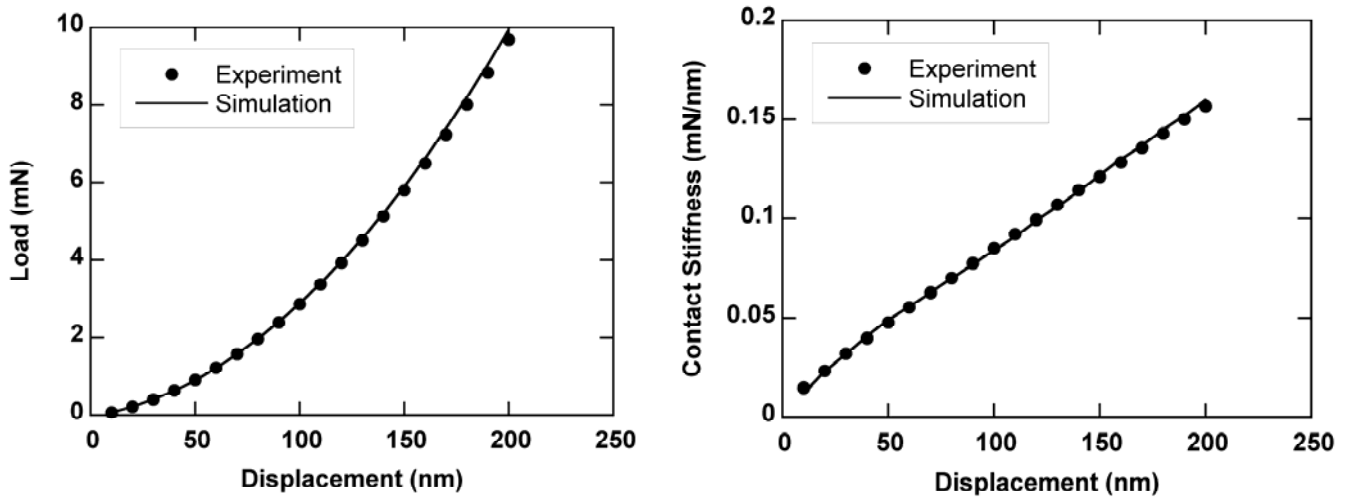


Fig. 7.5 Simulation results for silicon substrate calibration

Single layer properties and simulations

Similar to the silicon calibration tests, indentation tests into the single-layer ALD films were performed to determine the load and stiffness response. Using this indentation data, an iterative series of simulations was performed with variations in the yield stress from 2 to 6 GPa and a modulus range from 120 to 170 GPa. After multiple simulations, a best fit with $E_{fit} = 151.9 \pm 29.1$ GPa and $\sigma_{ys} = 5.2 \pm 1.3$ GPa, giving an indentation hardness of $H_{fit} = 12.1 \pm 3.2$ GPa (Figure 6.6). Similar simulations on the 50 nm ALD-tungsten, with a range in the yield stress from 5 to 7.5 GPa and in the modulus from 150 to 210 GPa, obtained a best fit using $E_{fit} = 204.9 \pm 46.5$ GPa and $\sigma_{ys} = 7.4 \pm 3.7$ GPa, resulting in an indentation hardness of $H_{fit} = 23.6 \pm 8.6$ GPa (Figure 6.7). These values compare well with previous nanoindentation experiments on thicker (200 nm) films of ALD-alumina and ALD-tungsten grown under similar conditions, where elastic modulus values of 145 GPa and 280 GPa and indentation hardness of 8 GPa and 18 GPa were observed (Moody et al. 2005).

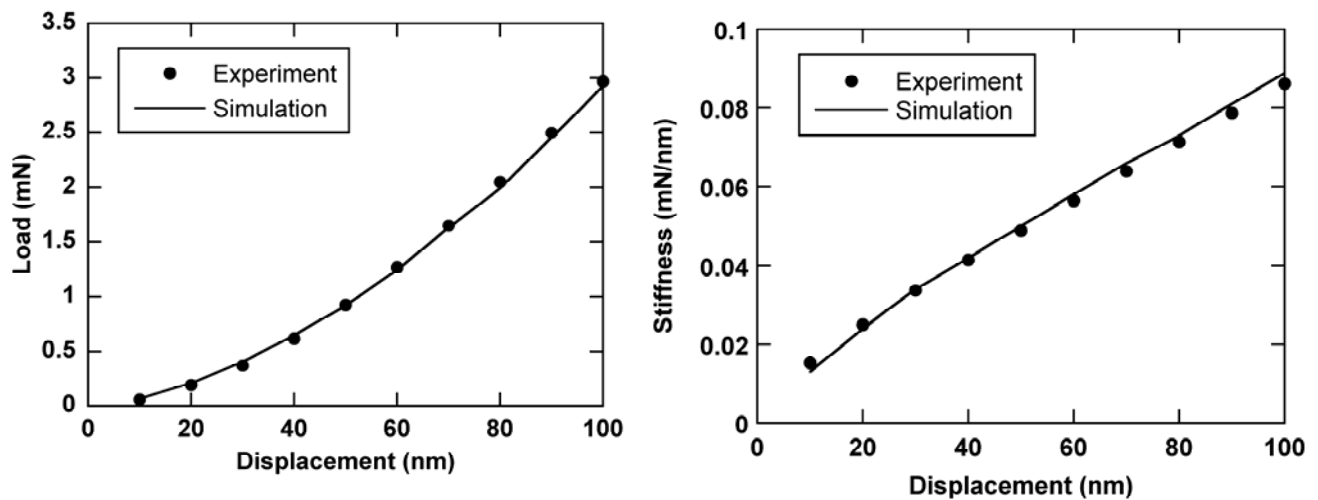


Figure 7.6 ALD-AIOx simulation results for 50 nm film on a silicon substrate. A best fit is obtained with $E = 151.9 \pm 29.1$, $\sigma_{ys} = 5.2 \pm 1.3$ and $H = 12.1 \pm 3.2$

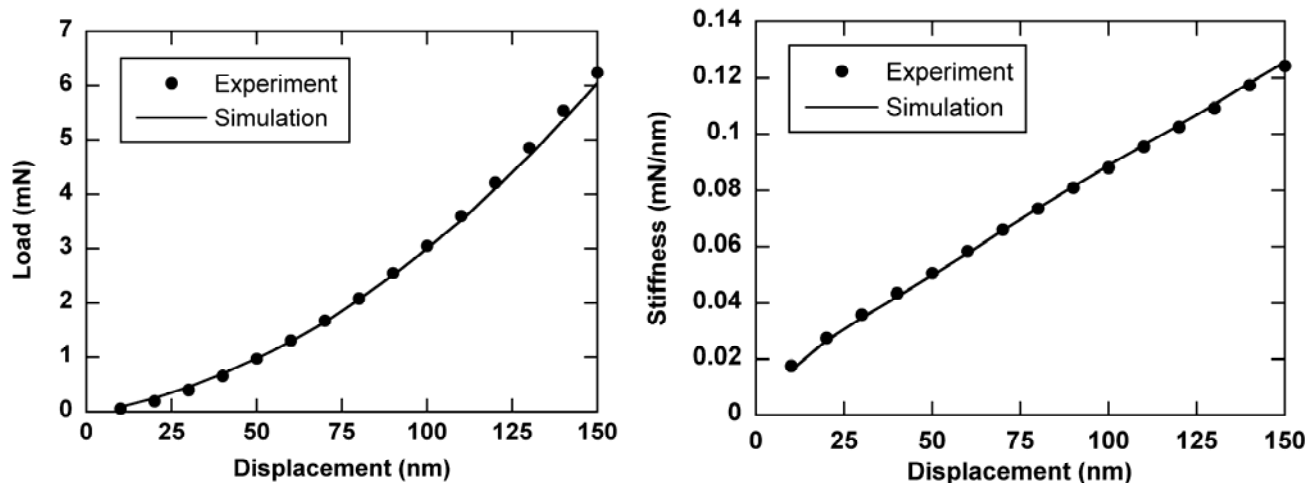


Figure 7.7. ALD-W simulation results for 50 nm film deposited on a silicon substrate. A best fit is obtained with $E = 204.9 \pm 46.5$, $\nu_{ys} = 7.4 \pm 3.7$ and $H = 23.6 \pm 8.6$.

Nanolaminate properties and simulations

In order to measure the thicknesses of the laminate stacks, TEM samples were cut from the nanolaminate using a focused ion beam (Figure 6.8). These results are shown in Table 6.1, where the composite film thicknesses range from 76.1 nm to 128.5 nm, rather than the expected 100 nm. Therefore, in order to normalize the substrate effect on the measured modulus and hardness, the indentation depth was normalized by the measured film thickness (Figure 6.9). The nanoindentation results show that the elastic modulus increased with decreasing number of bilayers. This is an expected trend, since with increasing volume fraction of the more rigid tungsten, one would expect (based on a rule of mixtures approach) a stiffer overall composite. Therefore, using a rule-of-mixtures approach and the values determined from the FEM modeling of the single layers, one would expect modulus values for the 4-, 8- and 16-bilayers modulus to be 193.6 GPa, 191.3 GPa and 184.1 GPa with indentation hardness of 21.2 GPa, 20.7 GPa and 19.1 GPa, respectively. This does not match well with the observed indentation data, where at shallow depths the modulus for the samples ranges from 145 to 180 GPa and the hardness varies from 5 to 7 GPa. This effect may be partially explained by the density gradient formed during the first 4 nm of film growth for the alumina and tungsten. If it is assumed that the first 4 nm have approximately 50% of the value of hardness and modulus for both the ALD alumina and tungsten, then the expected nanolaminate modulus values drop to 154.0 GPa, 133.8 GPa and 92.0 GPa for the 4-, 8- and 16-bilayer samples while the hardness drops to 17.2 GPa, 14.7 GPa and 9.6 GPa, respectively, which are closer to the observed values.

(a)

(b)

(c)

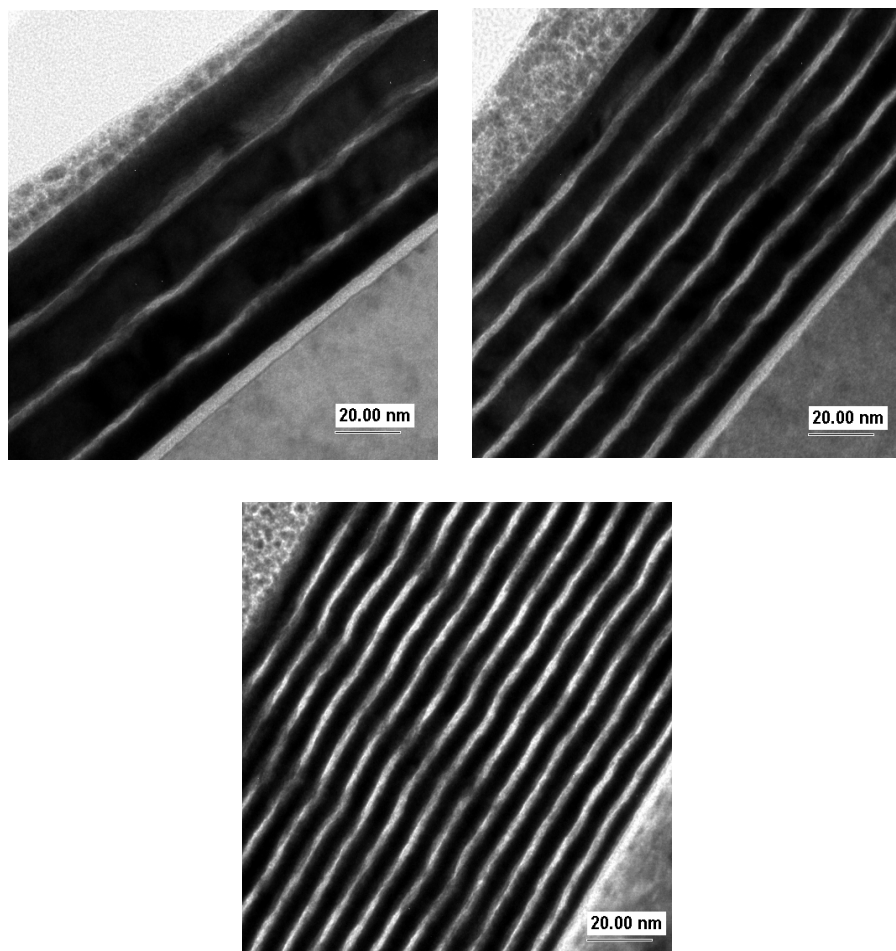


Figure 7.8. TEM images of ALD-nanolaminate cross-sections. The white layers are amorphous alumina and the darker layers are nanocrystalline tungsten. The thick white layer at the substrate is the native SiO_2 oxide layer. (a) 4-bilayer laminate stack (b) 8-bilayer nanolaminate and (c) 16-bilayer composite film.

Table 7.1 Bilayer thicknesses with average layer thicknesses. Note that with increasing number of bilayers the volume fraction of tungsten decreases.

*Typical error bars on the layer thickness measurements are $\pm 15\%$

# bilayers	Total thickness (nm)	Alumina layer thickness *	Tungsten layer thickness *	Tungsten volume fraction
4	76.1	5.0	14.0	78.8%
8	92.2	3.3	8.3	74.4%
16	128.5	3.3	4.8	60.7%

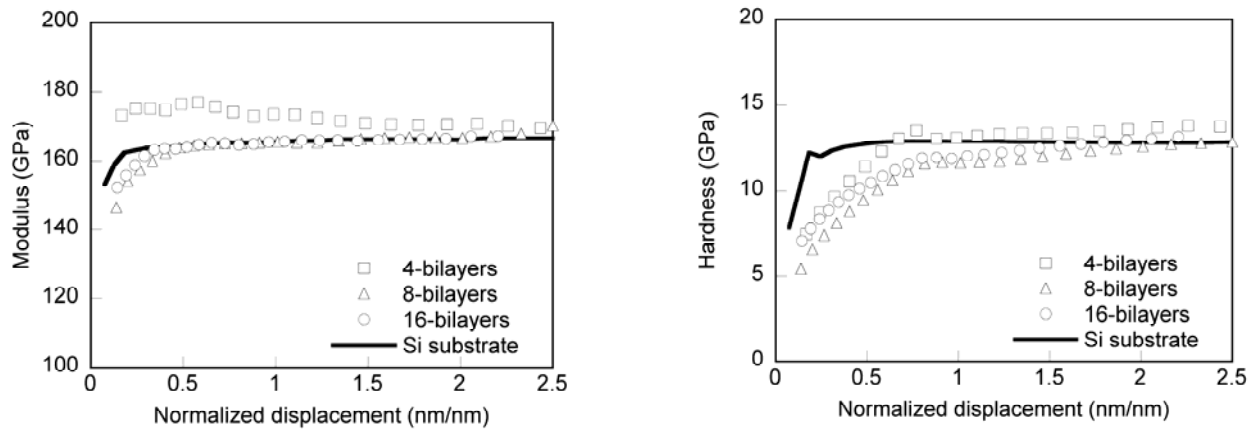


Figure 7.9. Normalized modulus and hardness for nanolaminate indentation tests on silicon substrate.

In order to generate the simulation mesh and material property input files for the nanolaminate films, a rule-of-mixtures approach was used. This was done in order to reduce the total number of elements and nodes, as a mesh where the elements were of the same size as a single layer was too large for the ABAQUS simulation to handle. For the nanolaminate mesh, rather than attempting to mesh each layer in the nanolaminate, the entire laminate thickness was meshed as a single film. Similarly, the elastic modulus and yield stress were determined from a rule-of-

mixtures, where the alumina was assumed to have the same mechanical values as determined from the single layer simulations, and the tungsten properties were varied to obtain a best fit to the experimental nanolaminate data. Using this approach, the best fits to the simulations were determined (Figure 6.10 – 6.12) and the results are given in Table 6.2; however, unlike the single layer simulations, where the model gave reasonable approximations of the measured ALD-film properties, it is apparent that the nanolaminate simulations failed to capture the indentation response with realistic nanolaminate layer properties. This failure of the simulation to accurately represent the observed mechanical behavior may be due to compaction of the non-dense films or, more likely, fracture or delamination of the laminated structure which led to a change in the system constraint and mechanical behavior.

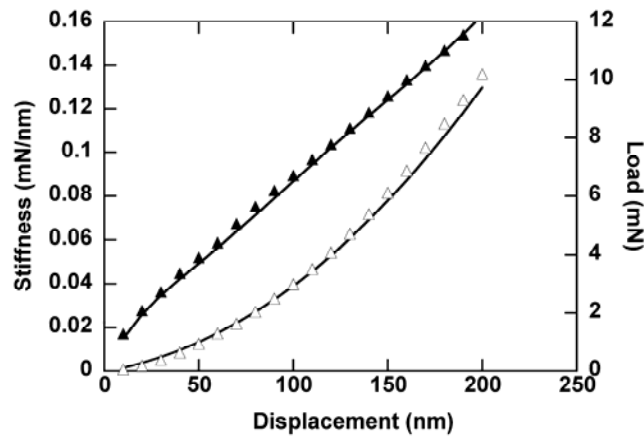


Figure 7.10 Simulation results for 4-bilayer nanolaminate with $E = 326$ GPa and $\gamma_s = 13.2$ GPa

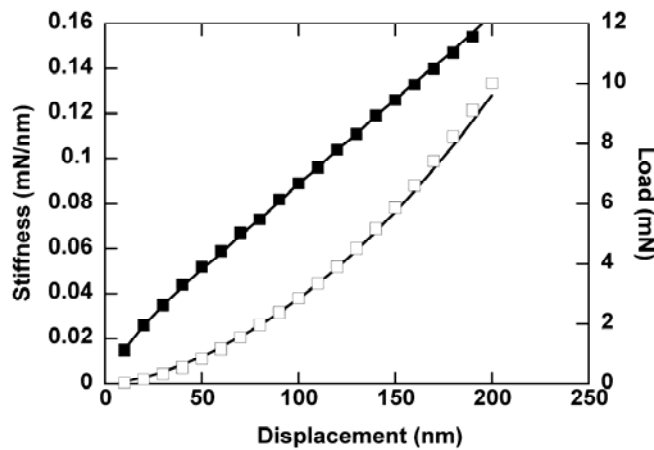


Figure 7.11 Simulation results for 8-bilayer nanolaminate where $E = 219$ GPa and $\gamma_s = 6.5$ GPa

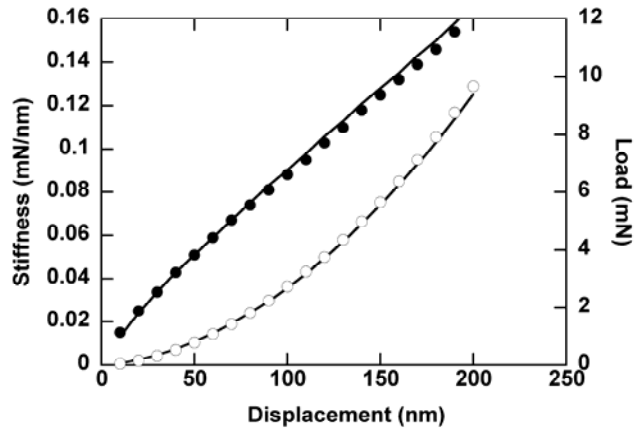


Figure 7.12 Simulation results for 16-bilayer sample where $E = 173$ GPa and $\sigma_{ys} = 3.8$ GPa

Table 7.2 Best-fit tungsten modulus (with constant ALD-alumina of $E = 151.9$ GPa and $\sigma_{ys} = 5.2$ GPa) for nanolaminates.

# bilayers	Tungsten yield stress (GPa)	Tungsten modulus (GPa)
4	13.2	326
8	6.5	219
16	3.8	173

Nanolaminate fracture response

Interestingly, during the indentation testing of the nanolaminates, displacement discontinuities in the loading were observed in the 8- and 16-bilayer samples at large indentation depths. These events most likely corresponded to either fracture or delamination within the nanolaminate stack. Images of indents (at a peak load of 9 mN), did show evidence of cracking in the laminates (Figure 6.13). This led to additional scratch tests using both a 100 nm radius Berkovich and 1 μ m radius conical tips in order to evaluate the fracture resistance of the nanolaminate films. Representative images from these scratch tests can be seen in Figure 6.14, where it is shown that for increasing number of bilayers the length of the cracks increase (corresponding to a decrease in the film fracture toughness). Additionally, it is shown that the Berkovich tip generates increased channel crack formation compared to the spherical tip. It is hypothesized that this is due to the higher tangential stresses produced by the Berkovich tip.

These higher tangential stresses result in a positive shift of the frictional coefficient, from 0.05 with a conical tip to slightly greater than 0.12 using the Berkovich, an increase of almost a factor of three.

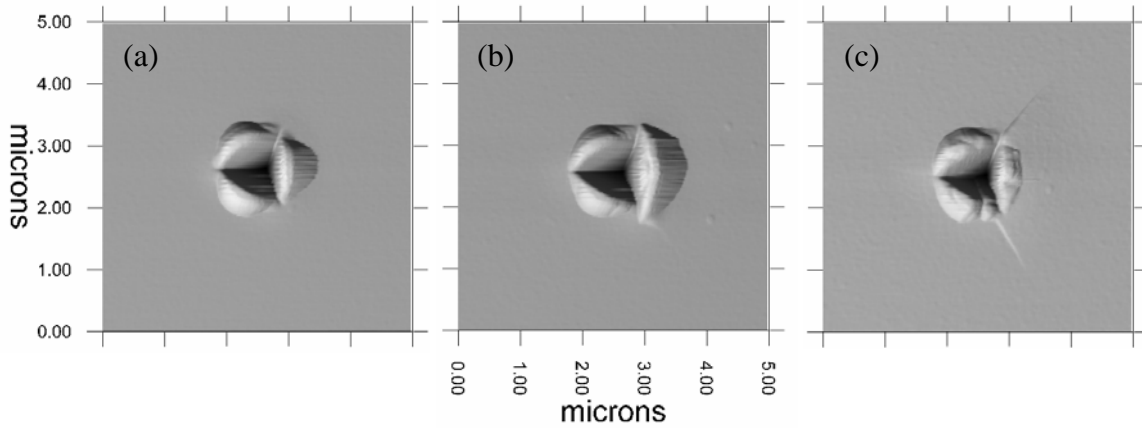


Figure 7.13. Scanning probe images showing indentation induced cracking the nanolaminates. (a) In the 4-bilayer film, there is only plastic pileup, while in (b) the 8-bilayer film small cracks can be seen starting at the indenter impression corners. (c) for the 16-bilayer sample, cracking can be easily seen extending from the corners of the indentation.

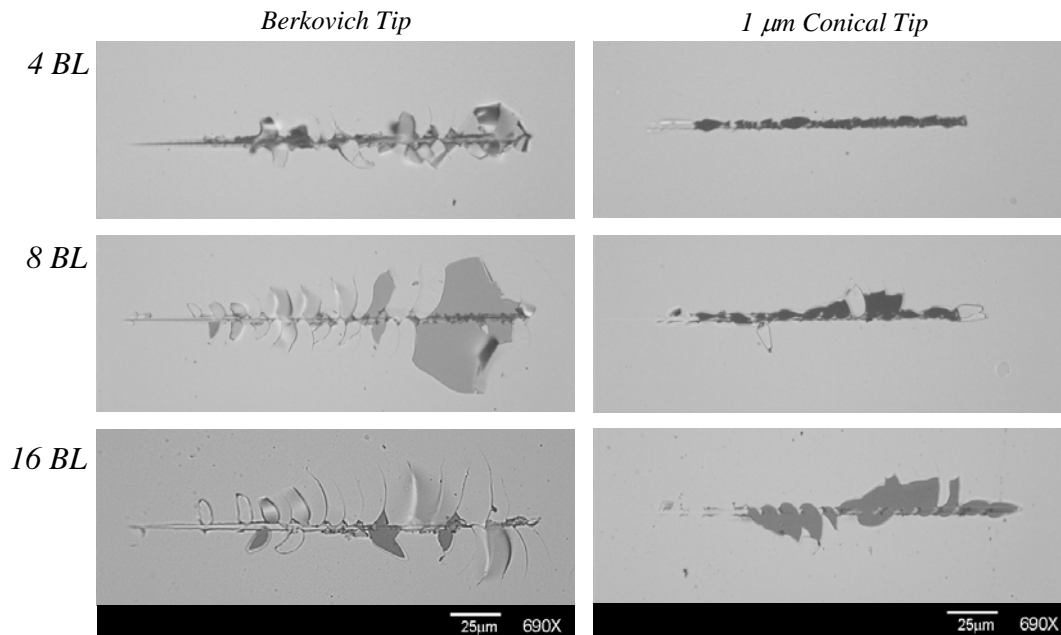


Figure 7.14. Scratch fracture and delaminations observed for both (a) Berkovich and (b) conical tips. The magnitude and extent of the fractures increases with decreasing layer period, and is noticeably larger for the Berkovich tip due to the increased lateral forces.

These results can be compared to the scratch behavior of single layer ALD tungsten and alumina films deposited onto silicon in a similar manner (Moody et al. 2004; Moody et al. 2005), where a 200 nm ALD-tungsten film deposited at 300 °C displayed significant film fracture and delamination (Figure 6.15). Therefore, in comparison to the single film, the same scratch test on ALD nanolaminates only produce small channel cracks that are localized near the scratch track and increase in magnitude as the normal and tangential loads increase. Interestingly, a strong reverse length scale is observed in the fracture behavior of the laminates, where it is seen that with decreasing layer period, the channel crack length increases. To describe this behavior, one could argue that the toughness of the composite film is directly related to the total volume fraction of metal, where the metal acts to absorb energy plastically. Using this rationale, the 16 bilayer system would have the lowest fracture toughness since it has the lowest overall volume fraction of metal as compared to the 4- or 8-bilayer systems. Consequently, this argument would also imply that a pure tungsten film would have the highest toughness when compared to the laminate films; however, this disagrees with the results of the single layer ALD-tungsten film (Moody et al. 2005). As a result, this implies that a maximum in the thin film fracture toughness exists between the geometry of a single blanket film of ALD-tungsten and the 4- bilayer laminated structure of ALD-tungsten and ALD-alumina.

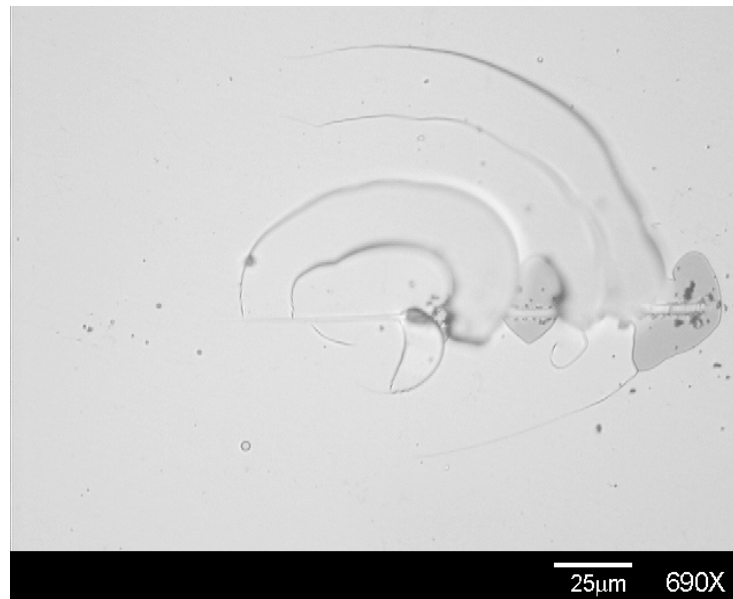


Figure 7.15. Fracture and delamination observed from scratch test of 200 nm ALD-tungsten film deposited at 300 °C. Notice that the scratch lengths are much larger than those of the nanolaminated ALD films.

Summary

A study finite element based study of atomic layer deposited samples composed of both blanket and nanolaminate-based ALD films using nanocrystalline tungsten and amorphous aluminum oxide was performed. Using this technique, it was determined that the elastic modulus and hardness of a 50 nm blanket ALD-alumina film was $E_{fit} = 151.9 \pm 29.1$ GPa, $\sigma_{ys} = 5.2 \pm 1.3$ GPa and $H_{fit} = 12.1 \pm 3.2$ GPa. The best fit for a 50 nm ALD-tungsten film was found with $E_{fit} = 204.9 \pm 46.5$ GPa, $\sigma_{ys} = 7.4 \pm 3.7$ GPa and $H_{fit} = 23.6 \pm 8.6$ GPa. When this same method was applied to the nanolaminate systems, the finite element model appeared to break down, likely corresponding to laminate film failure, which the model was unable to capture. Therefore, using the nanoindentation data at shallow displacements (where any substrate effect would be minimal) an elastic modulus and hardness range for 4- 8- and

16-bilayer systems of 284 to 183 GPa and 8.2 to 7.0 GPa respectively was measured. From nanoscratch tests, a strong reverse length-scale effect was observed in the fracture behavior of the laminated films. It was seen that as the layer period decreased, the apparent toughness of the film decreased. When these results are compared to similar tests on blanket films of ALD-tungsten, a maximum in the fracture toughness can be predicted with bilayer thicknesses somewhat larger than 21 nm of ALD-tungsten and 4 nm of ALD-alumina.

References

- Bhattacharya, A. K., and Nix, W. D. (1988). "Analysis of elastic and plastic deformation associated with indentation testing of thin films on substrates." *International Journal of Solids and Structures*, 24(12), 1287.
- Bourcier, R. J., Follstaedt, D. M., Dugger, M. T., and Myers, S. M. (1991). "Mechanical characterization of several ion-implanted alloys: nanoindentation testing, wear testing and finite element modeling." *Nuclear Instruments & Methods in Physics Research, Section B (Beam Interactions with Materials and Atoms)*, B59-B60(pt.2), 905.
- Cai, X., and Bangert, H. (1995). "Hardness measurements of thin films-determining the critical ratio of depth to thickness using FEM." *Thin Solid Films*, 264(1), 59.
- Callister, W. D. (1997). *Materials Science and Engineering: An Introduction*, John Wiley & Sons, Inc.
- Cameron, M. A., Gartland, I. P., Smith, J. A., Diaz, S. F., and George, S. M. (2000). "Atomic layer deposition of SiO₂ and TiO₂ in alumina tubular membranes: Pore reduction and effect of surface species on gas transport." *Langmuir*, 16(19), 7435.
- Costescu, R. M., Cahill, D. G., Fabreguette, F. H., Sechrist, Z. A., and George, S. M. (2004). "Ultra-Low Thermal Conductivity in W/Al₂O₃ Nanolaminates." *Science*, 303(5660), 989.
- Ferguson, J. D., Weimer, A. W., and George, S. M. (2000). "Atomic layer deposition of Al₂O₃ and SiO₂ on BN particles using sequential surface reactions." *Applied Surface Science*, 162, 280.
- Follstaedt, D. M., Knapp, J. A., and Myers, S. M. (2004). "Mechanical properties of ion-implanted amorphous silicon." *Journal of Materials Research*, 19(1), 338.
- Han, M., Luo, Y., Moryl, J. E., Osgood, R. M., Jr., and Chen, J. G. (1998). "A near-edge X-ray absorption fine structure study of atomic layer epitaxy: the chemistry of the growth of CdS layers on ZnSe(100)." *Surface Science*, 415(3), 251.
- Ishii, M., Iwai, S., Kawata, H., Ueki, T., and Aoyagi, Y. (1997). "Atomic layer epitaxy of AlP and its application to X-ray multilayer mirror." *Journal of Crystal Growth*, 180(1), 15.
- Klaus, J. W., Ferro, S. J., and George, S. M. (2000). "Atomically controlled growth of tungsten and tungsten nitride using sequential surface reactions." *Applied Surface Science*, 162-163, 479.
- Klaus, J. W., Ott, A. W., Dillon, A. C., and George, S. M. (1998). "Atomic layer controlled growth of Si₃N₄ films using sequential surface reactions." *Surface Science*, 418(1), 14-19.
- Klaus, J. W., Ott, A. W., Johnson, J. M., and George, S. M. (1997). "Atomic layer controlled growth of SiO₂ films using binary reaction sequence chemistry." *Applied Physics Letters*, 70(9), 1092.
- Knapp, J. A., and Follstaedt, D. M. (2004). "Hall-Petch relationship in pulsed-laser deposited nickel films." *Journal of Materials Research*, 19(1), 218.
- Knapp, J. A., Follstaedt, D. M., Barbour, J. C., and Myers, S. M. (1997). "Finite-element modeling of nanoindentation for determining the mechanical properties of implanted layers and thin films." *Nuclear Instruments & Methods in Physics Research, Section B: Beam Interactions with Materials and Atoms*, 127-128, 935.
- Knapp, J. A., Follstaedt, D. M., Myers, S. M., Barbour, J. C., and Friedmann, T. A. (1999). "Finite-element modeling of nanoindentation." *Journal of Applied Physics*, 85(3), 1460.
- Laursen, T. A., and Simo, J. C. (1992). "Study of the mechanics of microindentation using finite elements." *Journal of Materials Research*, 7(3), 618.
- Moody, N. R., Jungk, J. M., Kennedy, M. S., Prasad, S. V., Bahr, D. F., and Gerberich, W. W. "Mechanical Properties of Wear tested LIGA Nickel." *Fundamentals of Nanoindentation and Nanotribology III*, Boston, MA.
- Moody, N. R., Jungk, J. M., Mayer, T. M., Wind, R. A., George, S. M., and Gerberich, W. W. "Fracture of atomic layer deposited tungsten films." *11th International Conference on Fracture*, Turin, Italy.

Sneh, O., Clark-Phelps, R. B., Londergan, A. R., Winkler, J., and Seidel, T. E. (2002). "Thin film atomic layer deposition equipment for semiconductor processing." *Thin Solid Films*, 402(1-2), 248.

8. SUMMARY

In this project we have carried out an extensive program of process development, growth, and characterization of a variety of tribological coatings for MEMS devices. We have shown that ALD is well suited to deposition of friction and wear-reducing films on MEMS structures. Sequential reactant exposure and self-limiting surface chemistry result in exquisite control of deposition rate and film thickness, and extremely conformal coating of high aspect ratio structures. The challenge remains to examine the mechanical and tribological properties of thin ALD films, and their suitability to application in functional MEMS devices. Processes for preparation of a wide range of materials, which are potential hard and/or lubricious coatings, have been demonstrated by ALD. The ease of fabrication of alloys and nanolaminates of ALD materials adds extra dimensions to our ability to tailor the properties of materials for tribological applications.

We have shown that ALD is capable of depositing low friction ($\text{COF} \sim 0.02$) and conformal solid lubricant WS_2 films on high aspect ratio MEMS devices. Zn catalyzed adsorption and reaction of WF_6 greatly increases the growth. Coatings only tens of nm thick can give low friction and increase wear life since sliding is interfacial, i.e., between the transfer film and the wear track on the coating. The hexagonal crystal texture of ALD WS_2 is temperature dependent, but shear-induced reorientation at our high contact stresses assures low friction. The development of ALD solid lubricant films is expected to enable the application of low friction and low wear films to moving mechanical assemblies such as MEMS structures and REB devices.

W and W/ Al_2O_3 nanolaminate films were grown by ALD reactions of WF_6 and Si_2H_6 for W and $(\text{CH}_3)_3\text{Al}$ and H_2O for Al_2O_3 . For this study, two sets of nanolaminate films were grown on silicon and sapphire substrates. One set of nanolaminates had a total film thickness of 500 Å and films were grown which were composed of 2, 4, and 8 bilayers. The second set of nanolaminates had a total thickness of 1000 Å with films composed of 4, 8, and 16 bilayers. Nanolaminate films were grown on the alumina adhesion layer by alternating tungsten and alumina deposition. W nucleation on Al_2O_3 was found to be retarded, requiring 5 – 10 cycles of exposure to reach a steady state growth rate. In addition, surface roughness of the resulting W film was found to be dependent on the nucleation behavior. To explore this phenomenon, we carried out extensive nucleation measurements of W, and found nucleation kinetics and surface roughness to be primarily dependent on Si_2H_6 exposure. A hemispherical cap model of nucleation and coalescence was developed which qualitatively explains the observed morphological evolution.

We have conducted a systematic study of the mechanical property and fracture behavior of atomic layer deposited tungsten films as a function of film thickness. These films were deposited at 300°C creating a state of high residual tensile stress. Nanoindentation testing showed that elastic modulus and hardness increased with film thickness. For the thickest films, these values were substantially higher than the substrate values with the hardness equaling values for bulk and sputter deposited films. Nanoscratch tests were then used to study scratch adhesion. These tests triggered channel cracking and delamination in the thickest film. The cracks formed in succession parallel to the path of previous cracks. Corresponding film and interfacial fracture energies were determined using mechanics-based channel cracking and delamination models. For our film system, the analysis showed that film fracture occurred at an energy of 0.4 J/m². The corresponding interfacial fracture energy for film delamination between the channel cracks was 50 mJ/m² with a mode I component equal to 30 mJ/m². This value is less than the work of adhesion for sputter deposited tungsten films on silicon substrates but may accurately reflect the influence of lower film density along the substrate interface.

We have initiated a study of atomic layer deposited nanolaminate-based composites using alternating layers of nanocrystalline tungsten and amorphous aluminum oxide. Using nanoindentation techniques, we have determined that the elastic modulus and hardness range for 4- 8- and 16-bilayer systems from 284 to 183 GPa and 8.2 to 7.0 GPa respectively at shallow displacements. From nanoscratch tests, a strong reverse length-scale effect was observed in the fracture behavior of the laminated films. It was seen that as the layer period decreased, the apparent toughness of the film decreased. When these results are compared to similar tests on blanket films of ALD-

tungsten, a maximum in the fracture toughness can be predicted with bilayer thicknesses somewhat larger than 21 nm of ALD-tungsten and 4 nm of ALD-alumina.

A study finite element based study of atomic layer deposited samples composed of both blanket and nanolaminate-based ALD films using nanocrystalline tungsten and amorphous aluminum oxide was performed. Using this technique, it was determined that the elastic modulus and hardness of a 50 nm blanket ALD-alumina film was $E_{fit} = 151.9 \pm 29.1$ GPa, $\sigma_{ys} = 5.2 \pm 1.3$ GPa and $H_{fit} = 12.1 \pm 3.2$ GPa. The best fit for a 50 nm ALD-tungsten film was found with $E_{fit} = 204.9 \pm 46.5$ GPa, $\sigma_{ys} = 7.4 \pm 3.7$ GPa and $H_{fit} = 23.6 \pm 8.6$ GPa. When this same method was applied to the nanolaminate systems, the finite element model appeared to break down, likely corresponding to laminate film failure, which the model was unable to capture. Therefore, using the nanoindentation data at shallow displacements (where any substrate effect would be minimal) an elastic modulus and hardness range for 4- 8- and 16-bilayer systems of 284 to 183 GPa and 8.2 to 7.0 GPa respectively was measured. From nanoscratch tests, a strong reverse length-scale affect was observed in the fracture behavior of the laminated films. It was seen that as the layer period decreased, the apparent toughness of the film decreased. When these results are compared to similar tests on blanket films of ALD-tungsten, a maximum in the fracture toughness can be predicted with bilayer thicknesses somewhat larger than 21 nm of ALD-tungsten and 4 nm of ALD-alumina.

Distribution:

1	MS 9018	Central Technical Files, 8945-1
2	MS 0899	Technical Library
1	MS 0320	D. Chavez, LDRD Office
5	MS 0750	T. M. Mayer, 6118
1	MS 0889	T. W. Scharf, 1824
1	MS 0889	S. V. Prasad, 1824
1	MS 9409	N. R. Moody 8754
1	MS 1245	R. S. Goeke 2452
1	MS 0889	M. T. Dugger, 1824
1	MS 1245	R. K. Grubbs 2452
1	MS 1310	J. M. Jungk 1824
1	MS 1245	R. L. Poole 2452